

Image-based reconstruction for strong-nonlinear transient problems by using an Enhanced ReConNN

Yu Li^{a, *}, Hu Wang^{a, **}, Wenquan Shuai^a, Honghao Zhang^{b, c}, Yong Peng^{b, c}

a. State Key Laboratory of Advanced Design and Manufacturing for Vehicle Body, College of Mechanical and Vehicle Engineering, Hunan University, Changsha, 410082, PR China

b. Key Laboratory of Traffic Safety on Track of Ministry of Education, School of Traffic and Transportation Engineering, Central South University, Changsha 410000, PR China

c. Joint International Research Laboratory of Key Technology for Rail Traffic Safety, Central South University, Changsha, 410000, PR China

Abstract

With the improvement of pattern recognition and feature extraction of Deep Neural Networks (DNNs), more and more problems are attempted to solve from the view of images. Recently, a Reconstructive Neural Network (ReConNN) was proposed to obtain an image-based model from an analysis-based model, which can help us to solve many high frequency problems with difficult sampling, e.g. sonic wave and collision. However, due to the slight difference between simulated images, the low-accuracy of the Convolutional Neural Network (CNN) and poor-diversity of the Generative Adversarial Network (GAN) make the reconstruction process low-accuracy, poor-efficiency, expensive-computation and high-manpower. In this study, an improved ReConNN model is proposed to address the mentioned weaknesses. Through experiments, comparisons and analyses, the improved one is demonstrated to outperform in accuracy, efficiency and cost.

Keywords: EReConNN; Strong-nonlinear transient problem; Thin-walled metal structure; Reconstruction; Ordered-image-based.

Highlights

* First author. E-mail address: liyu_hnu@hnu.edu.cn (Y. Li)

** Corresponding author. Tel.: +86 0731 88655012; fax: +86 0731 88822051.

E-mail address: wanghu@hnu.edu.cn (H. Wang)

- i. An EReConNN is proposed to overcome the shortcomings of the existing ReConNN;
- ii. The EReConNN is successfully utilized to a highly nonlinear transient case;
- iii. An experiment of a collision process of a thin-walled structure is reconstructed well.

1. Introduction

It is well known to us that, with the explosive development of the Machine Learning (ML), some ML-based methods, including the Neural Network (NN) which is the core technology of the Deep Learning (DL), have been utilized to many interdisciplines, such as computational mechanics [1-6], heat transfer [7-10], fluid mechanics [11-14], etc. Moreover, with the improvements of pattern recognition and feature extraction of the DNNs, more and more researchers have attempted to solve some engineering problems from the view of images, e.g. Lin [15], Sosnovik [16], Yu [17] and Banga [18] et al used the CNN-based models to recognize and extract features of the initial designs of the topology optimization, and predicted the optimized structure. The testing results based on the Solid Isotropic Material with Penalization (SIMP) method validated that the CNN-based model could reduce plenty of time for the optimization. As to the problems of crack, Fan [19], Dung [20], Dorafshan [21], Cha [22], Chen [23], Yokoyama [24] and Tong [25] et al extracted features of crack images by using the DNNs. Through comparisons between the conventional edge detection and the DNN methods, the DNNs outperformed for the crack detection. Additionally, in regard to the material problems, Li [9] aimed at that the traditional methods to study effective thermal conductivities of composite materials were all based on developing a good physical understanding, so he utilized the pattern recognition of the CNN to infer the effective thermal conductivities of the composite materials. Cang [26] proposed a generative model that created an arbitrary amount of artificial material samples when trained on only a limited amount of authentic samples. The key contribution of this work was the introduction of a morphology constraint to the training of the generative model, that enforced the

resultant artificial material samples to have the same morphology distribution as the authentic ones. As for some other fields, Wang [27] proposed a novel full closed-loop approach to detect and classify power quality disturbances based on a deep CNN, and the field data from a multi-micro grid system were used to further prove the validity of the proposed method.

Recently, a ReConNN was proposed as a reconstructive model with a distinctive characteristic framework "from analysis-based models to image-based models". It was developed in Ref. [28] and further applied to a heat transfer problem of a 3D Plate Fin Heat Sink (PFHS) in Ref. [29]. The ReConNN model was attempted for physical field reconstructions and to construct more objective and more information included models. However, not only the ReConNN proposed in Ref. [28], but also the ReConNN slightly improved in Ref. [29] were all at the exploratory stage considering the accuracy, efficiency and cost. Some shortcomings in the existing ReConNN are described and analyzed as follows.

i. The ReConNN was mainly composed of the CNN and the GAN. The CNN was employed to construct the mapping from the images to the objective functions, while the GAN was utilized to generate more similar images. Nevertheless, because most of the research problems were optimization or convergence problems, the differences between simulated images, which were used as training samples, were slight. This phenomenon caused the accuracy of the CNN was not very satisfied, and the diversity of the generated images by the GAN was not also very good;

ii. As shown in Figs. 1 (a) and (b), the design domains of both the topology optimization and the PFHS are fixed during the optimization or calculation process. These weak-nonlinear problems could be handled easily by the ReConNN. While as for strong-nonlinear transient problems, such as the collision problem as shown in Fig. 1 (c), the ReConNN was powerless;

iii. During the ReConNN, a distinct characteristic of both the CNN and GAN was big data, meaning expensive simulations. However, the ReConNN mainly aimed at those whose samples were hardly obtained, if the necessary samples were too many, the study would be meaningless;

iv. At the end of the reconstruction work by the ReConNN, it needed the interpolation algorithm to complete the reconstruction. Nevertheless, as mentioned in the 1st shortcoming, the low-accuracy of the CNN and poor-diversity of the GAN would influence the reconstruction results. Furthermore, the matching between interpolated objective functions and generated images would also consume a lot of manpower.

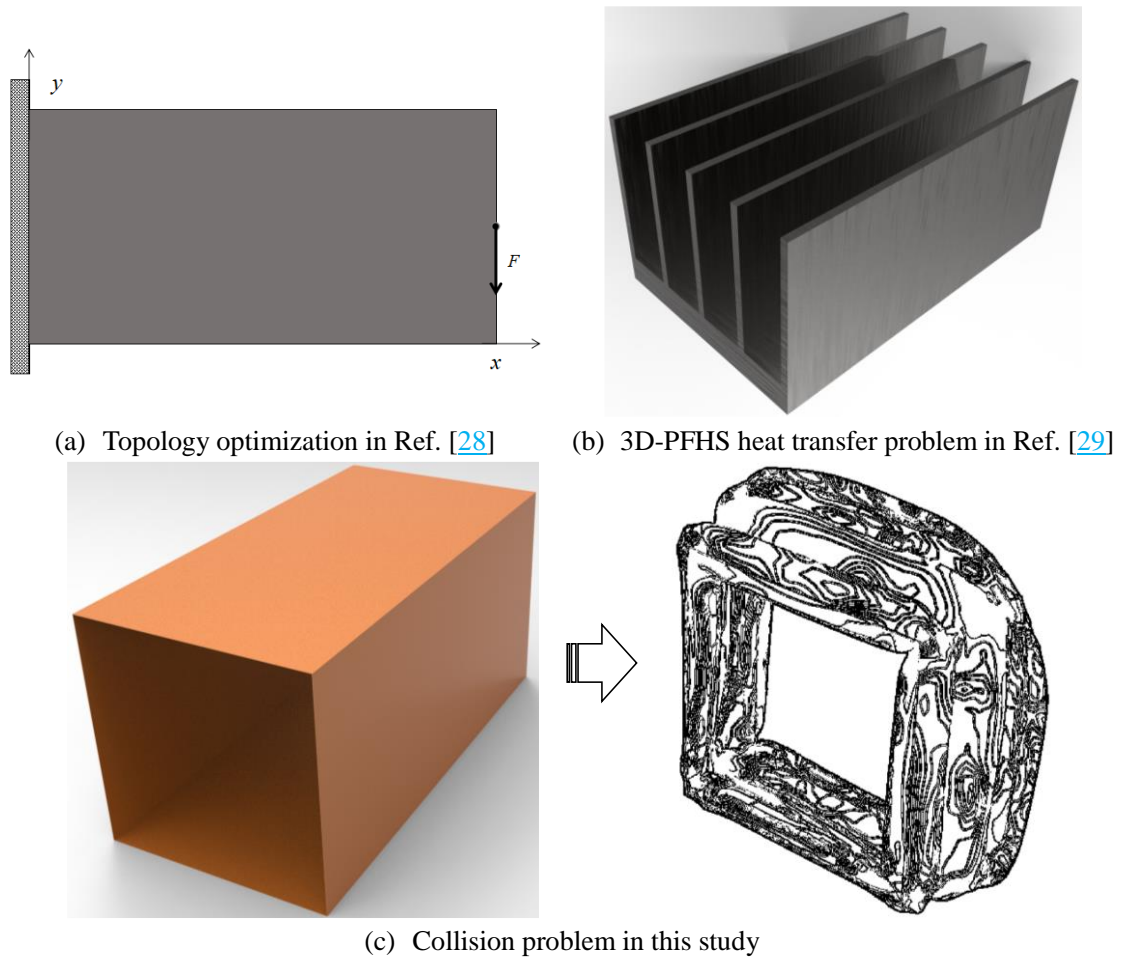


Fig. 1. Degree comparisons of nonlinearity between different problems.

In order to address above mentioned shortcomings, this study proposes an Enhanced ReConNN (EReConNN) model, which abandons the previous the integration architecture of the CNN and GAN, and uses an Adversarial Variational Autoencoder (AVAE) model to realize the reconstruction. Through tests, comparisons and experiments, whether for accuracy and efficiency, or for strong-nonlinear problems, the EReConNN is improved greatly.

The remainder of this study is organized as follows. In Section 2, the basic idea of the collision problem is introduced. Subsequently, Section 3 is devoted to show the structure of the EReConNN, meanwhile the reason why the CWGAN is not very suitable for this study is also analyzed. Then the detailed numerical examples, results, and analyses are presented in Section 4 to demonstrate the effectiveness of the proposed EReConNN. In Section 5, the EReConNN is utilized to an actually engineering problem, a collision process of a combined multi-cell thin-walled aluminum structure. Ultimately, some perspective remarks are provided in the final section to conclude the paper.

2. Problem descriptions

2.1. Physical model

The 3D Computer Aided Design (CAD) model of the collision problem is presented in Fig. 2. The collision body is a cuboid whose material is Al alloy 6,061-T6 as shown in Table 1, and defined with an initial velocity v_0 along the negative direction of z -axis. Furthermore, a point mass of $300kg$ is coupled in the center of the other side of the collision surface, which is marked by a red cross.

Table 1 The material parameters of the Al alloy 6,061-T6.

Parameter	Value	
Young's modulus (MPa)	71,275	
Poisson's ratio	0.33	
Yield stress (MPa)	241.5	
Density (t/mm^3)	2.9×10^{-9}	
Hardening curve	Yield stress (MPa)	Plastic deformation
	241.5	0
	263.0	0.0069
	278.8	0.0217
	318.8	0.0921
	346.7	0.1408
	374.5	0.1914
	388.8	0.2181
	423.8	0.2862
	464.3	0.3728

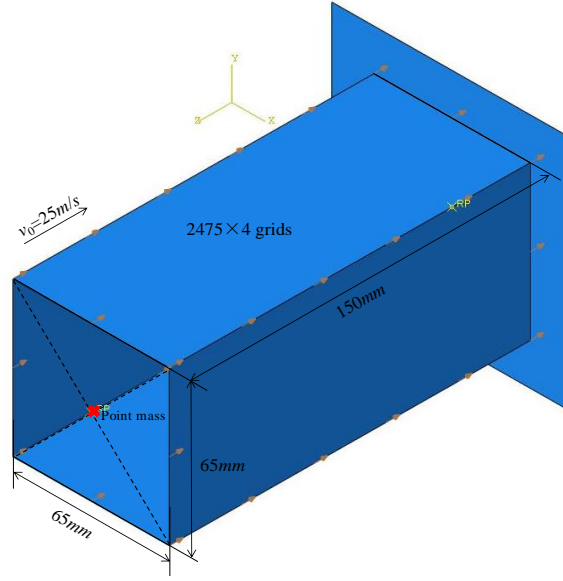


Fig. 2. The CAD model of the collision problem.

2.2. Mathematical model

In the collision process, work is done by the external forces during the deformation. If there is no heat loss, the work will be all converted into the strain energy.

$$U = A \quad (1)$$

The strain energy of per unit volume can be represented by

$$U_0 = U_0(\varepsilon_x, \varepsilon_y, \varepsilon_z, \gamma_{xy}, \gamma_{yz}, \gamma_{zx}) \quad (2)$$

s.t.

$$\gamma_{xy} = \frac{1}{G} \tau_{xy}, \gamma_{yz} = \frac{1}{G} \tau_{yz}, \gamma_{zx} = \frac{1}{G} \tau_{zx} \quad (3)$$

where

$$G = \frac{E}{2(1+\nu)} \quad (4)$$

where A is the work done by the external forces; U is the strain energy; ε is the strain; E and ν are the Young's modulus and the Poisson's ratio to define the elastic properties, respectively; τ is the shear stress; and G is the shear modulus.

The distortion and destroy of the collision body generally contain two stages, elastic deformation and plastic deformation. When the body is in the elastic-plastic

stage, the stress and strain are not corresponding to each other yet. The equation of strain compatibility of a 3-dimensional elastic-plastic is calculated by

$$\left\{ \begin{array}{l} \frac{\partial^2 \varepsilon_x}{\partial y^2} + \frac{\partial^2 \varepsilon_y}{\partial x^2} = \frac{\partial^2 \gamma_{xy}}{\partial x \partial y} \\ \frac{\partial^2 \varepsilon_y}{\partial z^2} + \frac{\partial^2 \varepsilon_z}{\partial y^2} = \frac{\partial^2 \gamma_{yz}}{\partial y \partial z} \\ \frac{\partial^2 \varepsilon_z}{\partial x^2} + \frac{\partial^2 \varepsilon_x}{\partial z^2} = \frac{\partial^2 \gamma_{zx}}{\partial z \partial x} \\ 2 \frac{\partial^2 \varepsilon_x}{\partial y \partial z} = \frac{\partial}{\partial x} \left(-\frac{\partial \gamma_{yz}}{\partial x} + \frac{\partial \gamma_{xz}}{\partial y} + \frac{\partial \gamma_{xy}}{\partial z} \right) \\ 2 \frac{\partial^2 \varepsilon_y}{\partial z \partial x} = \frac{\partial}{\partial y} \left(-\frac{\partial \gamma_{yz}}{\partial x} + \frac{\partial \gamma_{xz}}{\partial y} + \frac{\partial \gamma_{xy}}{\partial z} \right) \\ 2 \frac{\partial^2 \varepsilon_z}{\partial x \partial y} = \frac{\partial}{\partial z} \left(-\frac{\partial \gamma_{yz}}{\partial x} + \frac{\partial \gamma_{xz}}{\partial y} + \frac{\partial \gamma_{xy}}{\partial z} \right) \end{array} \right. \quad (5)$$

The simplest form of linear elasticity is the isotropic case, and the stress-strain relationship is given by

$$\begin{bmatrix} \varepsilon_x \\ \varepsilon_y \\ \varepsilon_z \\ \gamma_{xy} \\ \gamma_{xz} \\ \gamma_{yz} \end{bmatrix} = \begin{bmatrix} 1/E & -\nu/E & -\nu/E & 0 & 0 & 0 \\ -\nu/E & 1/E & -\nu/E & 0 & 0 & 0 \\ -\nu/E & -\nu/E & 1/E & 0 & 0 & 0 \\ 0 & 0 & 0 & 1/G & 0 & 0 \\ 0 & 0 & 0 & 0 & 1/G & 0 \\ 0 & 0 & 0 & 0 & 0 & 1/G \end{bmatrix} \begin{bmatrix} \sigma_x \\ \sigma_y \\ \sigma_z \\ \sigma_{xy} \\ \sigma_{xz} \\ \sigma_{yz} \end{bmatrix} \quad (6)$$

where σ is the stress.

In the plastic stage, the characteristics of the stress and strain are nonlinear and no-uniqueness, the state of the strain is related to not only the stress, but also the change history of the stress. The plastic constitutive relation can be represented as

$$\left\{ \begin{array}{l} d\varepsilon_x^p = \frac{d\varepsilon_i}{\sigma_i} \left[\sigma_x - \frac{1}{2}(\sigma_y + \sigma_z) \right], d\varepsilon_{xy}^p = \frac{3}{2} \frac{d\varepsilon_i}{\sigma_i} \tau_{xy} \\ d\varepsilon_y^p = \frac{d\varepsilon_i}{\sigma_i} \left[\sigma_y - \frac{1}{2}(\sigma_x + \sigma_z) \right], d\varepsilon_{yz}^p = \frac{3}{2} \frac{d\varepsilon_i}{\sigma_i} \tau_{yz} \\ d\varepsilon_z^p = \frac{d\varepsilon_i}{\sigma_i} \left[\sigma_z - \frac{1}{2}(\sigma_x + \sigma_y) \right], d\varepsilon_{zx}^p = \frac{3}{2} \frac{d\varepsilon_i}{\sigma_i} \tau_{zx} \end{array} \right. \quad (7)$$

It can be further shorted as the Levy-Mises function.

$$d\boldsymbol{\varepsilon}_{ij}^p = \frac{3}{2} \frac{d\varepsilon_i}{\sigma_i} \mathbf{S}_{ij} \quad (8)$$

s.t.

$$\mathbf{S}_{ij} = \begin{bmatrix} \sigma_x - \sigma_m & \tau_{xy} & \tau_{xz} \\ \tau_{yx} & \sigma_y - \sigma_m & \tau_{yz} \\ \tau_{zx} & \tau_{zy} & \sigma_z - \sigma_m \end{bmatrix} \quad (9)$$

where

$$\sigma_m = \sigma_1 + \sigma_2 + \sigma_3 \quad (10)$$

where ε^p is the plastic strain increment; and \mathbf{S}_{ij} is the deflection stress tensor or stress deviator.

2.3. Implicit algorithm for dynamic problems

The dynamic problems mainly research the dynamic response of the structure in basic motions or under the dynamic forces. Currently, Newmark- β method [30] is one of the most widely used implicit algorithms for dynamical systems with arbitrary excitation.

The initial structural equations of motions for a linear system with dynamic forces is calculated by

$$M_0 \ddot{r}(t) + C_0 \dot{r}(t) + K_0 r(t) = F_0(t) \quad (11)$$

where M_0 , C_0 , and K_0 are the initial mass, damping and stiffness matrices, respectively; $\ddot{r}(t)$, $\dot{r}(t)$ and $r(t)$ are the functions of time t for nodal displacement, the nodal velocity and the nodal acceleration, respectively; and $F_0(t)$ is the initial load vector of nodal force with arbitrary excitation.

In order to compute the initial structural dynamic response by the Newmark- β method need to assemble the M_0 , C_0 , and K_0 at first. Then the $\dot{r}(t)$ and $r(t)$ can be obtained, and the initial nodal acceleration is represented by

$$\ddot{r}(0) = M_0^{-1} [F_0(0) - C_0 \dot{r}(0) + K_0 r(0)] \quad (12)$$

After that, the following related coefficients can be inferred by time step Δt and parameters γ and β .

$$\begin{aligned}
a_0 &= \frac{1}{\beta \Delta t^2}, a_1 = \frac{\gamma}{\beta \Delta t}, a_2 = \frac{1}{\beta \Delta t}, a_3 = \frac{1}{2\beta} - 1, \\
a_4 &= \frac{\gamma}{\beta} - 1, a_5 = \Delta t \left(\frac{\gamma}{2\beta} - 1 \right), a_6 = \Delta t (1 - \gamma), a_7 = \gamma \Delta t
\end{aligned} \tag{13}$$

Finally, the effective stiffness matrix \tilde{K}_0 can be presented by

$$\tilde{K}_0 = K_0 + a_0 M_0 + a_1 C_0 \tag{14}$$

As for each time step, the effective load vector \tilde{F} at $t + \Delta t$ is

$$\tilde{F}(t + \Delta t) = F_0(t + \Delta t) + M_0 [a_0 r(t) + a_1 \dot{r}(t) + a_2 \ddot{r}(t)] + C_0 [a_1 r(t) + a_4 \dot{r}(t) + a_5 \ddot{r}(t)] \tag{15}$$

The correspondingly nodal displacement r , nodal acceleration \ddot{r} and nodal velocity \dot{r} are by Eqs. (16) - (18).

$$r(t + \Delta t) = \frac{\tilde{F}_0(t + \Delta t)}{\tilde{K}_0} \tag{16}$$

$$\ddot{r}(t + \Delta t) = a_0 [r(t + \Delta t) - r(t)] - a_2 \dot{r}(t) - a_3 \ddot{r}(t) \tag{17}$$

$$\dot{r}(t + \Delta t) = \dot{r}(t) + a_6 \ddot{r}(t) + a_7 \ddot{r}(t + \Delta t) \tag{18}$$

3. The architecture of the proposed EReConNN

Be different from the ReConNN whose main tasks are image regression (Convolution in Convolution, CIC) and image generation (Compressed Wasserstein GAN, CWGAN), the EReConNN is mainly composed of feature extraction of the physical field, physical field reconstruction and visualization enhancement by using the AVAE and Conditional GAN (CGAN), respectively.

As shown in Fig. 3, in Step i, the contour image of each iteration during the simulation is collected. In this study, the mappings of zOy and $x=y=z$ are chosen as the subjects investigated, respectively. Then the AVAE is employed to extract the features of the physical field in Step ii. After that, the feature values are interpolated to obtain more features in Step iii. Subsequently, all features are decoded by the decoder of the AVAE trained in Step ii orderly to complete the reconstruction. Finally, the CGAN is applied to enhance the visualization of the reconstruction and make the decoded

images more similar to the actual simulation results.

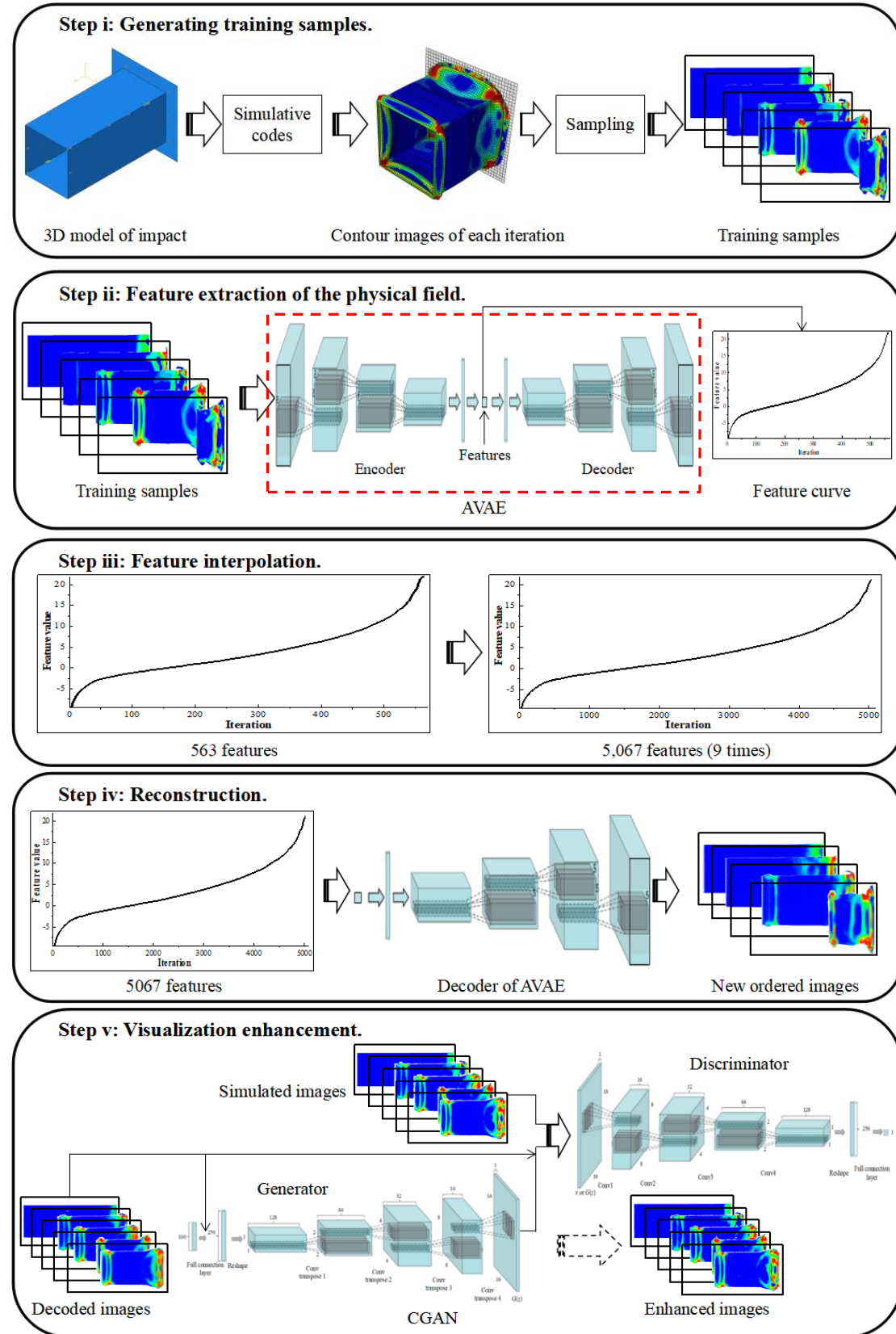


Fig. 3. The architecture of the EReConNN model.

3.1. Bilinear Interpolation

The pixel sizes of each simulated image are $480 \times 960 \times 3$ and $785 \times 880 \times 3$ when mapping on the surfaces of the xOy and $x=y=z$, respectively. In order to improve the universality of the algorithm, each image is re-sized to one of $256 \times 256 \times 3$ by using the Bilinear Interpolation.

In mathematics, the Bilinear Interpolation is an extension of the Linear Interpolation for interpolating functions of two variables (e.g., x and y) on a rectilinear 2D grid. The key idea is to perform linear interpolation first in one direction, and then again in another direction. Although each step is linear in the sampled values and in the position, the interpolation as a whole is not linear but rather quadratic in the sample location.

If a point (x, y) of an unknown function $f(x)$ is interpolated through another four points $Q_{11}=(x_1, y_1)$, $Q_{12}=(x_1, y_2)$, $Q_{21}=(x_2, y_1)$ and $Q_{22}=(x_2, y_2)$, the linear interpolation in the x -direction is first done and this yields

$$f(x, y_1) \approx \frac{x_2 - x}{x_2 - x_1} f(Q_{11}) + \frac{x - x_1}{x_2 - x_1} f(Q_{21}) \quad (19)$$

$$f(x, y_2) \approx \frac{x_2 - x}{x_2 - x_1} f(Q_{12}) + \frac{x - x_1}{x_2 - x_1} f(Q_{22}) \quad (20)$$

After that, the interpolation in the y -direction is processed to obtain the desired estimate.

$$\begin{aligned} f(x, y) &\approx \frac{y_2 - y}{y_2 - y_1} f(x, y_1) + \frac{y - y_1}{y_2 - y_1} f(x, y_2) \\ &= \frac{y_2 - y}{y_2 - y_1} \left(\frac{x_2 - x}{x_2 - x_1} f(Q_{11}) + \frac{x - x_1}{x_2 - x_1} f(Q_{21}) \right) \\ &\quad + \frac{y - y_1}{y_2 - y_1} \left(\frac{x_2 - x}{x_2 - x_1} f(Q_{12}) + \frac{x - x_1}{x_2 - x_1} f(Q_{22}) \right) \\ &= \frac{1}{(x_2 - x_1)(y_2 - y_1)} \left(f(Q_{11})(x_2 - x)(y_2 - y) + f(Q_{21})(x - x_1)(y_2 - y) \right. \\ &\quad \left. + f(Q_{12})(x_2 - x)(y - y_1) + f(Q_{22})(x - x_1)(y - y_1) \right) \\ &= \frac{1}{(x_2 - x_1)(y_2 - y_1)} \begin{bmatrix} x_2 - x & x - x_1 \end{bmatrix} \begin{bmatrix} f(Q_{11}) & f(Q_{12}) \\ f(Q_{21}) & f(Q_{22}) \end{bmatrix} \begin{bmatrix} y_2 - y \\ y - y_1 \end{bmatrix} \end{aligned} \quad (21)$$

3.2. Adversarial Variational Autoencoder

An Autoencoder (AE) [31] is a feed-forward NN which is trained to approximate the identity function. That is, it is trained to map from a vector of values to the same vector. When it is used for dimensionality reductions, the first half of the network (encoder) is a model which maps from high-dimensional to low-dimensional spaces, and the second half (decoder) maps from low-dimensional to high-dimensional spaces. Compared with the AE, the outputs from the encoder in the VAE [32, 33] have two purposes, one represents the mean of a Gaussian distribution (z_{mean}, μ^2), and another means the logarithmic value for the variance of a Gaussian distribution ($z_{\text{log_var}}, \log \sigma^2$). The input to the decoder can be calculated by

$$z = \mu^2 + \varepsilon \cdot \exp\left(\frac{\log \sigma^2}{2}\right) \quad (22)$$

where $\varepsilon \sim N(0, 1)$.

The optimized objective mainly includes two parts, one is the Mean Square Error (MSE) calculated by Eq. (23). The smaller the MSE, the more similar the predicted values and real samples. Besides, the Kullback–Leibler (KL) divergence, represented by Eq. (24), is employed to constraint the z_{mean} and $z_{\text{log_var}}$. Therefore, another is the KL divergence. The optimized objective is to minimize the weighted summation of the MSE and the KL expressed by Eq. (25).

$$MSE = \frac{1}{n} \sum (y - \hat{y})^2 \quad (23)$$

$$KL = 1 + \log \sigma^2 - \mu^2 - \sigma^2 = 1 + \log \sigma^2 - \mu^2 - \exp(\log \sigma^2) \quad (24)$$

$$L_{VAE} = 0.5MSE - 0.5KL \quad (25)$$

where y is the training sample; \hat{y} is the predicted value; and n is the sample size.

In this study, in order to improve the abilities of image restoration and feature extraction, the adversarial algorithm is added to the VAE. The improved VAE is named as AVAE and illustrated in Fig. 4. Similar to the GAN, a discriminator is added to the VAE. Through the judgement whether the input to the discriminator is real or fake, the decoded images by the VAE can be further improved. As shown in Table 2,

the encoder, decoder and discriminator mainly contain 6 convolutional or up sampling layers, respectively. A batch norm layer is added to each convolutional layer to normalize the data and improve training speed except the last convolutional layer in the discriminator. In the encoder, after the convolutional process, a full connection layer is used to obtain the features of required dimension. Meanwhile, a dropout layer is employed to the decoder and the discriminator to avoid the overfitting problem. The loss of the discriminator is calculated by

$$L_D = \mathbb{E}(D(x)) - \mathbb{E}[D(G(z))] \quad (26)$$

where x is the image from training samples; and z is a noise vector.

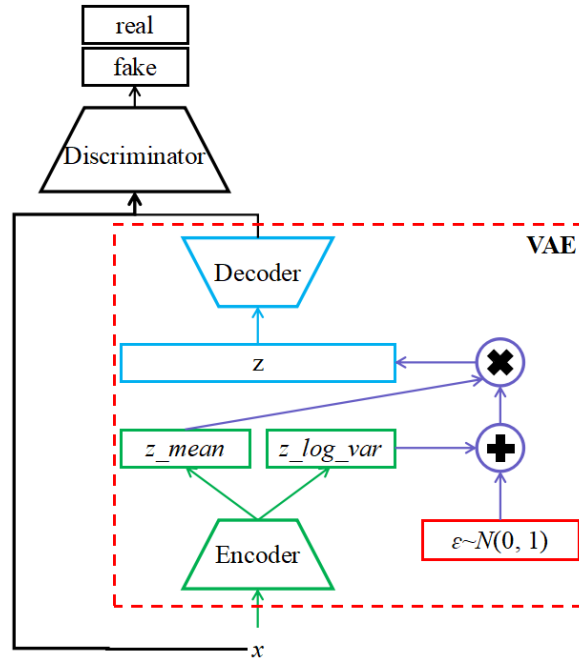


Fig. 4. The architecture of the AVAE.

Table 2 The detailed architecture parameters of the AVAE.

	Layer	Kernel size	Kernel stride	Output deep
Encoder	Conv-Batchnorm 1	4×4	2	32
	Conv-Batchnorm 2	4×4	2	32×2
	Conv-Batchnorm 3	4×4	2	32×4
	Conv-Batchnorm 4	4×4	2	32×8
	Conv-Batchnorm 5	4×4	2	32×16
	Conv-Batchnorm 6	4×4	2	32
Decoder	Full connection	Output nodes = Feature dimension		
	Full connection	Output nodes = 512		
	Up sampling-Dropout 1	4×4	2	32×16

	Up sampling-Dropout 2	4×4	2	32×8
	Up sampling-Dropout 3	4×4	2	32×4
	Up sampling-Dropout 4	4×4	2	32×2
	Up sampling-Dropout 5	4×4	2	32
	Up sampling	4×4	2	3
	Conv-Batchnorm 1	4×4	2	32
	Conv-Batchnorm 2	4×4	2	32×2
	Conv-Batchnorm 3	4×4	2	32×4
Discriminator	Conv-Batchnorm 4	4×4	2	32×8
	Conv-Batchnorm 5	4×4	2	32×16
	Conv-Dropout	4×4	2	1

3.2.1. The analyses of the powerless of the CWGAN in the ReConNN.

Compared with the EReConNN, the generative model of the ReConNN is the CWGAN. Meanwhile, through tests, the CWGAN might be powerless for a strong-nonlinear case in this study. The main reasons for the unsatisfactory results are discussed as follows.

- Firstly, as mentioned by Goodfellow, training GANs requires finding a Nash equilibrium [34] of a non-convex game with continuous and high-dimensional parameters. However, only when the function is convex, the Gradient Descent (GD) algorithm can realize the Nash equilibrium, which means the GAN can not reach the Nash equilibrium every training. Simultaneously, there is no a good way to achieve the Nash equilibrium at present;

- The GAN is defined as a min-max problem without loss functions, so the direction of the training process is difficultly determined whether is right. Moreover, the learning of the GAN is easily collapsed, such as this case, which causes the generator degenerate, the generated points same, and training stop;

- Importantly, compared with other generative models, e.g. VAE, the GAN uses a Gaussian or uniform distribution, rather than a assumed distribution, to approximate the real data as much as possible in theory. However, if the input image is too large, too many pixels will make the GAN uncontrollable, and this is why the images were compressed by a VAE of the CWGAN in Ref. [29];

- Nevertheless, although the compressed images by the VAE become small, the

input to the GAN is changed from an image data to a discrete data. In the GAN, the output from the generator passes a Softmax layer [35] by Eq. (27). The Softmax regression changes the input to a probability distribution. While the final output will be a matrix of one-hot. In the ML, one-hot is a group of bits among which the legal combinations of values are only those with a single high (one) bit and all the others low (zero) [36]. However, the discriminator might give a same judgement for different inputs, which causes the GAN not suit to learn a discrete data. For example, the one-hot matrices of (0.2, 0.3, 0.1, 0.2) and (0.2, 0.25, 0.2, 0.1) are both (0, 1, 0, 0). Furthermore, Jensen-Shannon (JS) divergence [37] by Eqs. (28) and (29) is used as the training objective of the GAN, and it is also not inappropriate to address a discrete data. Despite the WGAN has replaced the JS divergence by the Wassertein distance [38] by Eq. (30), the ability to learn a discrete data is still limited.

$$\text{softmax}(y_i) = y'_i = \frac{e^{y_i}}{\sum_{i=1}^n e^{y_i}} \quad (27)$$

$$JS(P\|Q) = \frac{1}{2}KL\left(P(x)\left\|\frac{P(x)+Q(x)}{2}\right.\right) + \frac{1}{2}KL\left(Q(x)\left\|\frac{P(x)+Q(x)}{2}\right.\right) \quad (28)$$

s.t.

$$KL(P\|Q) = \sum P(x) \log \frac{P(x)}{Q(x)} \quad (29)$$

$$W(P_1, P_2) = \inf_{\gamma \sim \Gamma(P_1, P_2)} \mathbb{E}_{(x,y) \sim \gamma} [\|x - y\|] \quad (30)$$

where $[y_1, y_2, \dots, y_i]$ is a input tensor to the Softmax layer, and $\Gamma(P_1, P_2)$ denotes the collection of all measures with marginals P_1 and P_2 on the first and second factors, respectively.

3.2.2. The analyses of the powerful of the AVAE in the EReConNN.

Essentially, the AVAE is a manifold learning model. There are two main distinguishing features of the manifold learning, one is the nonlinear dimensionality reduction, and another is describing the data characterization.

As for the dimensionality reduction, high-dimensional data, meaning data requiring more than two or three dimensions to represent, can be difficult interpreted.

One approach to simplification is to assume that the data of interest lie on an embedded nonlinear manifold within the lower-dimensional space. If the manifold is of low enough dimension, the data can be visualized in the low-dimensional space.

With respect to the data characterization, it means the things can represent the essential of the data. The manifold learning “remembers” the data through “learning” the data characterization which is similar to the human brain.

All these two features can help the AVAE outperforms in this study. As shown in Fig. 5, each image is regarded as a data point and each pixel is a dimension, so an image is a $m \times n$ -dimensional point in the Euclidean space. Besides, because all images in the data set only have one degree of freedom (DOF) of time, these images can be distributed in a 1-dimensional space. In addition, if the manifold is learned by the AVAE, the linear relation between local points in the low-dimensional space is the same as the one in the high-dimensional space, namely both have the character of $x=w_1x_1+w_2x_2+\dots+w_ix_i$. Thus, through trimming (interpolation) the data in the low-dimensional manifold space, meaningful and reasonable data in high-dimensional space can be obtained.

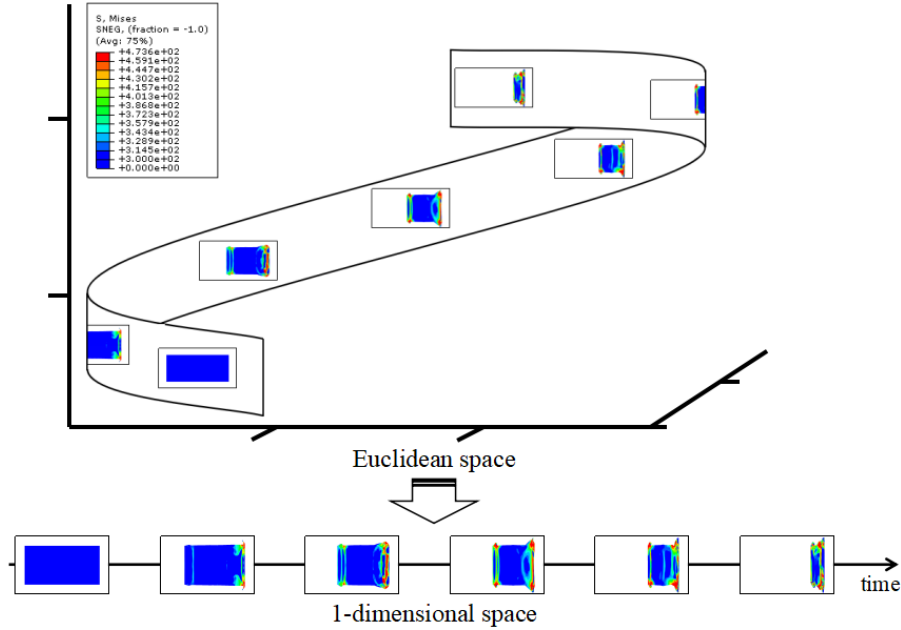


Fig. 5. The diagrammatic sketch of the manifold learning.

By the way, the GAN is difficult to infer another pixel through a pixel, and it can

generate all pixels only at one time. On the contrary, as for the VAE, the images in the manifold space are relevant to each other, so it is possible to generalize to new examples by a form of interpolation. Herein, through the interpolation of the extracted features, the new images in the high-dimensional manifold space can be generated and the amount of codes and computational cost can be largely saved. To sum up, as for ordered image set, the generation of the AVAE outperforms.

3.3. Conditional Generative Adversarial Network

The disadvantage of small samples for the AVAE is the accuracy reduction of the decoded images, so it is necessary to do image post-processing. Currently, there are many methods to increase the resolutions of images, such as Super-Resolution GAN (SRGAN) [39], SRCNN [40], Deep Reconstruction-Classification Network (DRCN) [41], Efficient Sub-Pixel CNN (ESPCN) [42], etc. However, these methods may not be suitable for this problem because the mentioned methods aim to reconstruct high-resolution using low-resolution images, e.g. the SRGAN can increase 4 times resolutions. While, the purpose of this section is to make the decoded images more similar to the actual simulated results without changing resolutions.

In this study, the CGAN is employed to enhance the visualization results. As shown in Fig. 6, the GAN [43] is a powerful generative model and a class of method to learn a data distribution $P_{model}(x)$ and realize a model to sample from it. The GAN is consisted of two functions, generator $G(z)$ which maps a sample depending on a random or a Gaussian distribution to the data distribution, and discriminator $D(x)$ which determines if an input belongs to the training data set. The generator and discriminator are typically learned jointly by alternating the training of $D(x)$ and $G(z)$ based on game theory principles. Mathematically, the training process can be described as

$$\min_G \max_D V(D, G) = \mathbb{E}_{x \sim P_{data}} [\log D(x)] + \mathbb{E}_{z \sim P_z} [\log (1 - D(G(z)))] \quad (31)$$

where x is the image from training samples P_{data} , z is a noise vector sampled from distribution P_z .

As shown in Fig. 6, the CGAN [44] is an extension of GAN where both the $G(z)$

and $D(x)$ receive an additional conditioning variable c , yielding $G(z, c)$ and $D(x, c)$. This formulation allows $G(z)$ to generate images conditioned on c . The c can be based on multiple information, e.g. classification labels [45], partial data for image restoration [46] or data from different modalities [44]. Mathematically, the optimized objective of the CGAN is represented by

$$\min_G \max_D V(D, G) = \mathbb{E}_{x \sim P_{data}} [\log D(x|c)] + \mathbb{E}_{z \sim P_z} [\log (1 - D(G(z|c)))] \quad (32)$$

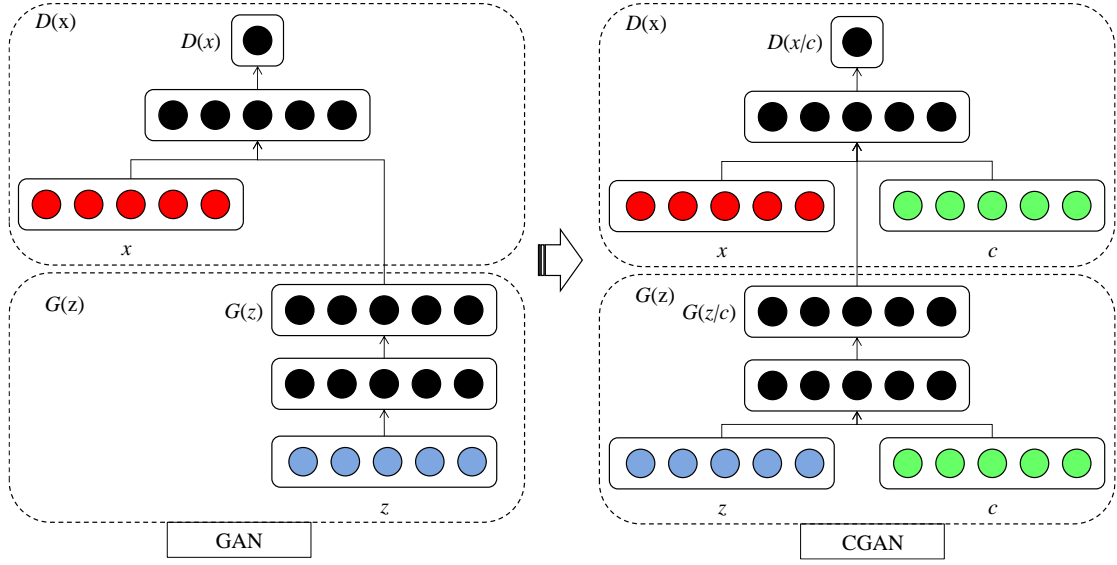


Fig. 6. The architectures of the GAN and the CGAN.

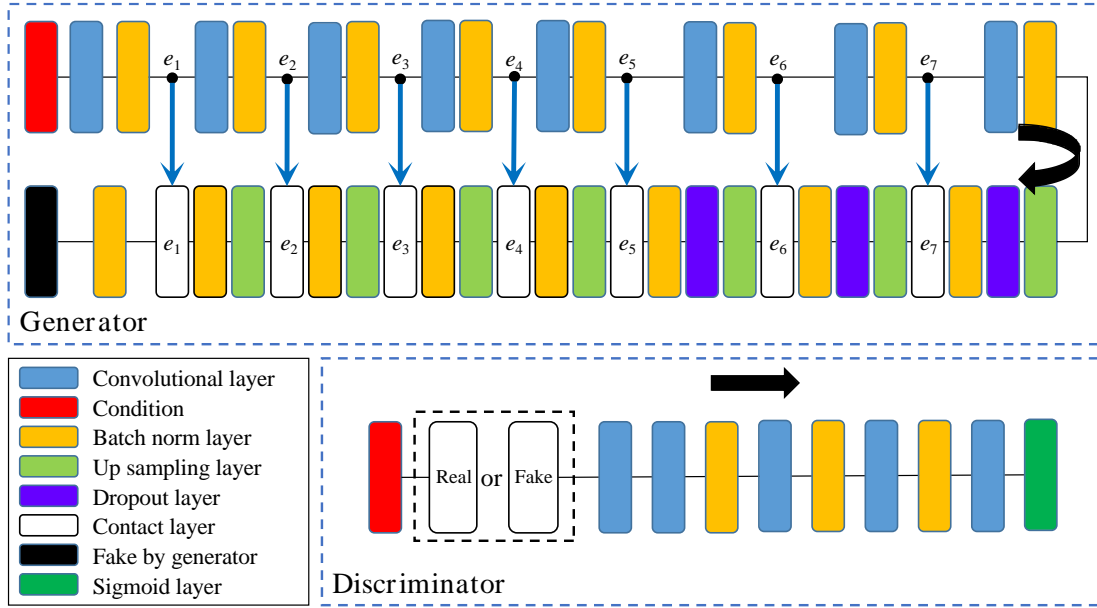


Fig.7. The detailed structure of the CGAN used in this study.

Additionally, the detailed structure of the CGAN in this study is shown in Fig. 7.

It can be seen that the condition is as the input to all of the generator and discriminator. In the generator, it looks like an AE. Firstly, the condition is convoluted, and the convoluted result of each layer will be contacted to the corresponding up sampling layer. Thus, the generator can generate a fake image according to the condition. The contact layer contacts the two tensors in the deep direction of the images, namely the final dimension of the data. The structure of the discriminator is similar to the convolutional architecture of the generator.

4. Tests and analyses

In the previous sections, the CAD model of the collision case and the enhanced reconstructive model are suggested. In order to evaluate the performance of the EReConNN, experiments, comparisons and analyses are presented in this section. In order to represent the reconstruction comprehensively, two mappings on the surfaces of xOy and $x=y=z$ are reconstructed, respectively.

4.1. The reconstruction of the mapping on the xOy surface

The mapping on the xOy surface of the 3D collision problem looks more like a 2D case. From this mapping surface, the computational ability requirements of VAE and CGAN are relative low.

4.1.1. Feature extraction of the physical field.

In this section, the dimension of the strong-nonlinear transient case is to be reduced and its essential features will be extracted. Therefore the first and most important issue is to make sure what's the suitable dimension of the features. As shown in Fig. 8, with the convolutional layers, the linear features of the physical field whose acceleration is $2.013 \times 10^7 m/s^2$, stress is $473.6 MPa$ and strain is 195.195 , are gradually extracted to map the physical field from high-dimensional to low-dimensional spaces. In this section, the dimensions of features are designed as 4, 64, 256 and 784, and the average VAE losses of total data set for each epoch are

shown in Fig. 9. Each case is trained 844,950 iterations, namely 150 epochs¹, and the simulation iterations are 5,633². It can be seen that when the dimension is less than 256, the loss values are not very difference. Although we can't easily summarize the lower the feature dimension, the smaller the VAE loss, at least it is demonstrated that it might be a good choice to use a low-dimensional feature.

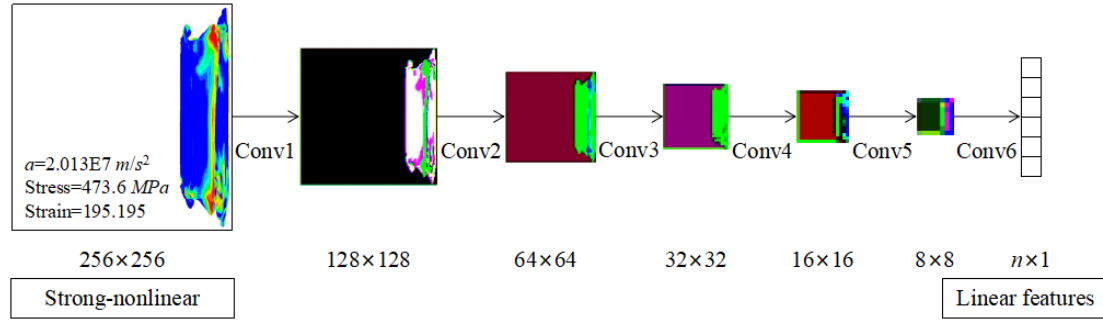


Fig. 8. The process of the feature extraction by the manifold learning.

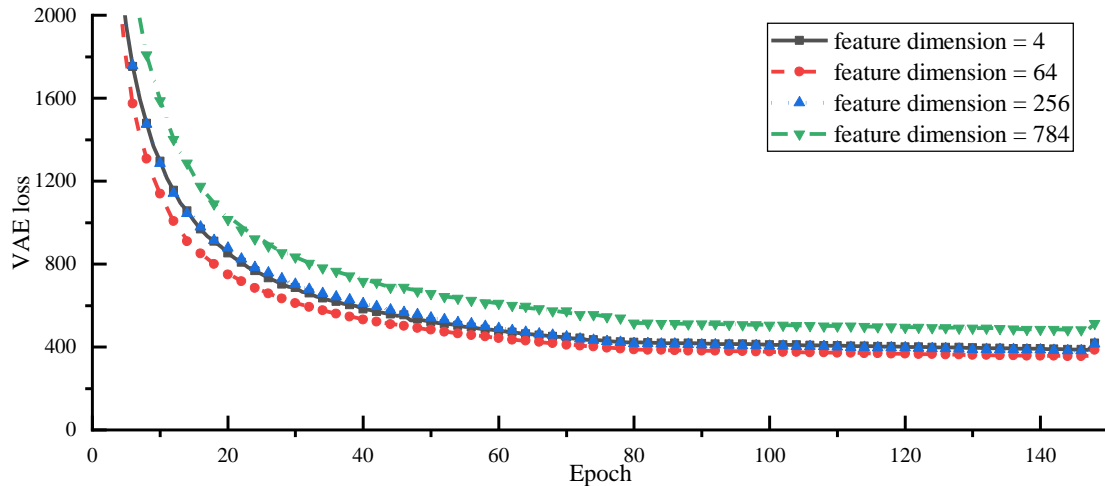


Fig. 9. The average VAE losses during the training processes for different feature dimensions for the cube mapping on xOy surface.

Meanwhile, according to the working thought of the ReConNN, after the dimensionality reduction, the WGAN is used to learn and generate the similar characteristic distributions of the physical field, and then the trained VAE is applied to decode the new generated features. The generated physical fields by using the CWGAN for the 4 different feature dimensions are shown in Fig. 10. It is found that no matter what is the dimension of the features, the new physical fields lack

¹ In one epoch, all samples should have been trained once.

² Thus the data set contain 5,633 physical field images.

convincing details and suffer blurred regions, which make them neither realistic enough nor have sufficiently high resolution.

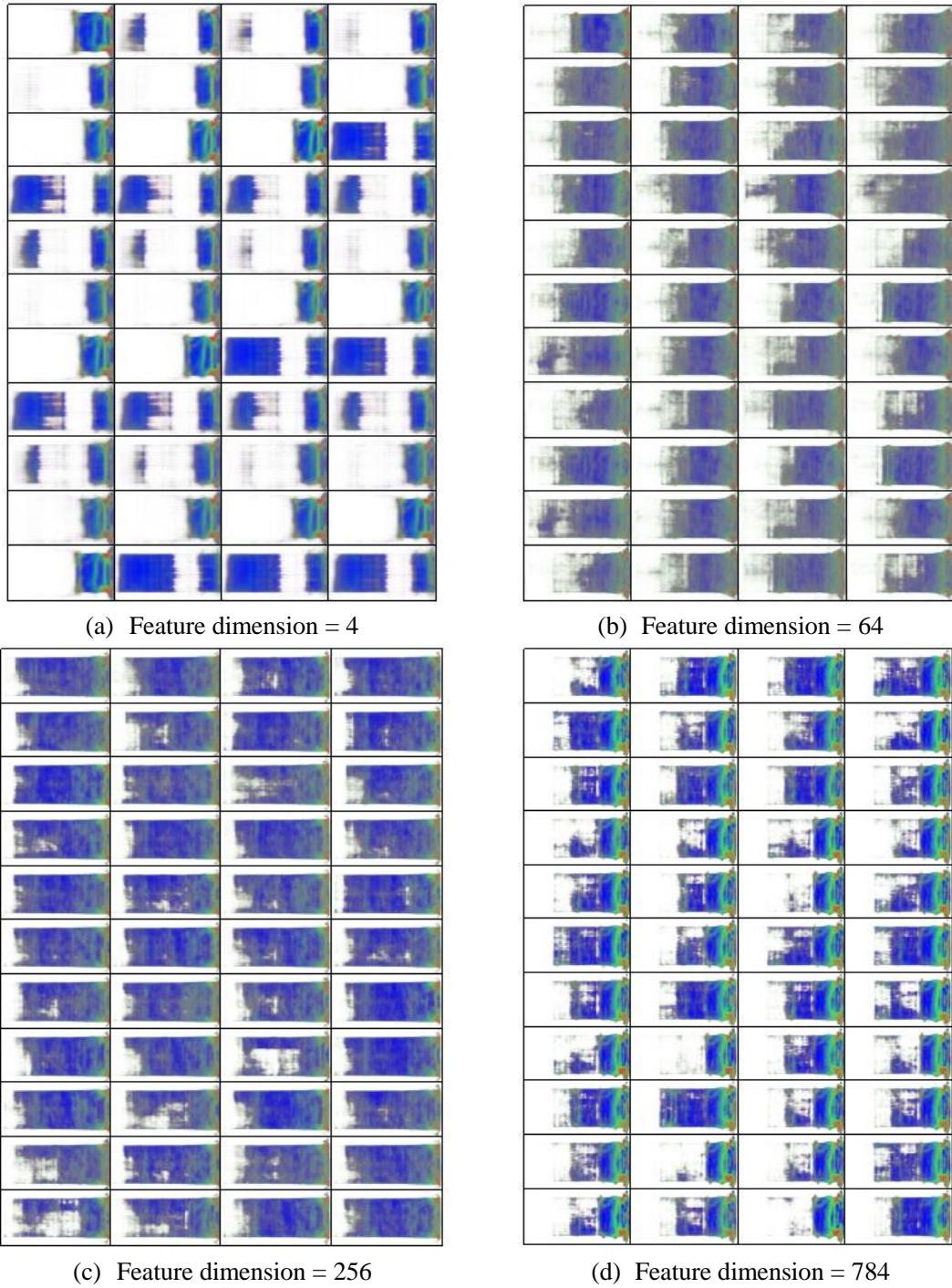


Fig. 10. Generated results by using the CWGAN in the ReConNN.

Actually, the physical quantities affecting the acceleration, stress, strain and others during the collision process are many and different, but all of them are time related. Accordingly, the DOF of the strong-nonlinear transient collision process is

regarded as one, namely the time. Therefore, the dimension of features is attempted to 1, and different iteration steps of the simulation, 281, 563, 1,126, 2,817 and 5,633, are run³, respectively. The average VAE losses during the training process are shown in Fig. 11. Of course, the purpose of this comparison dose not just judge the influence of the sample size on the training result which is well-known to us all. Due to that this study mainly focuses on those engineering problems whose data are hardly obtained or computational/simulation cost is too expensive. The less the necessary simulation iterations, the more meaningful the study. As shown in Fig. 11, it can be seen that the difference of the VAE losses between by using 281 samples and 5,633 samples is more than 4,000. Considering the gap of 20 times simulation iterations, the difference of 4,000 might be acceptable.

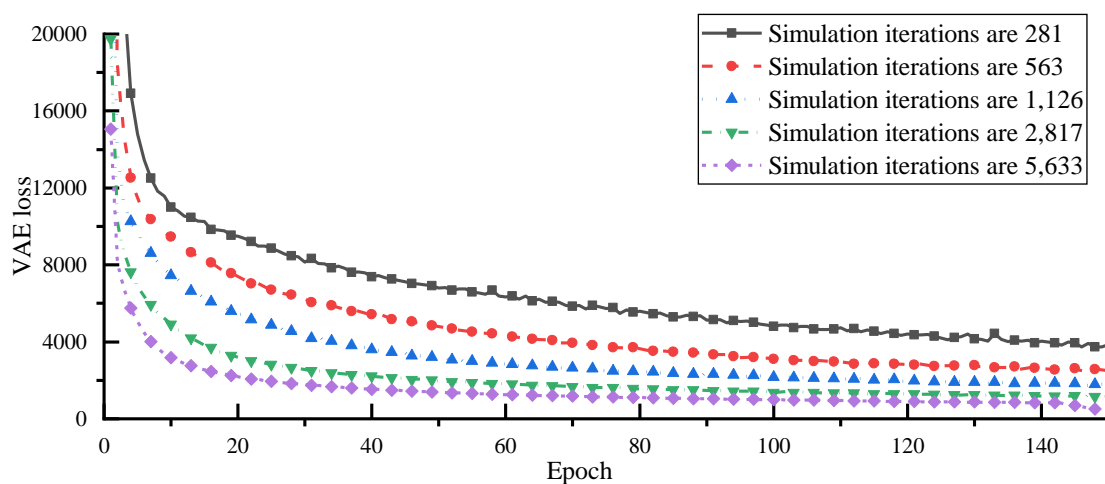


Fig. 11. The average VAE losses during training process when simulating different iterations for the cube mapping on xOy surface.

To further visualize the training results of the AVAE by using different iterations, the decoded physical fields in several collision iterations are represented in Table 3. Luckily, no matter what the total iterations of the simulation is, the AVAE can decode features well and restore the overall structure. To better observe and compare different results, enlarged images in the 5,000th iteration are presented in Table 4, respectively. It can be inferred that with the increase of the sample size, the decoded results are more similar to the actual simulation results. However, as for the results only

³ In this way, 281, 563, 1,126, 2,817 and 5,633 training samples can be obtained, respectively.

simulating 281 iterations, due to the limitation of sample size, the decoded image is very vague and lack convincing details, especially in the areas marked by rectangles. For the results by 5,633 samples in turn, 20 times simulation iterations truly improves the decoded results. Nevertheless, the images are still vague, and though the detailed features have been improved, it is not satisfied yet. Therefore, no matter what is the simulation iteration, the follow-up work for image improvements is necessary and this will be introduced detailedly in the following Section 4.1.3.

Table 3 The decoded physical fields when simulating different iterations for the cube mapping on xOy surface.

where the units of the a and stress are m/s^2 and MPa , respectively.

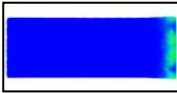
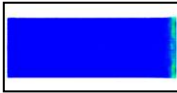



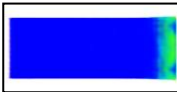




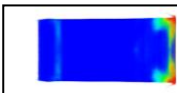



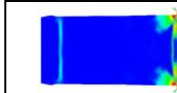
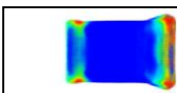
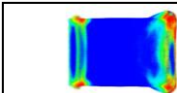
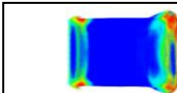
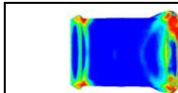
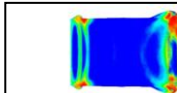
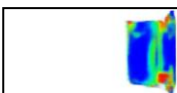


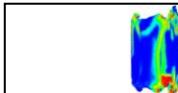

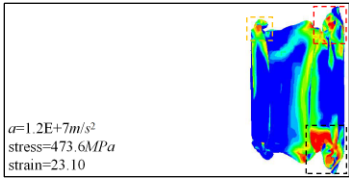
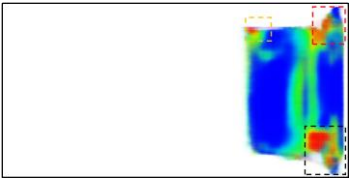
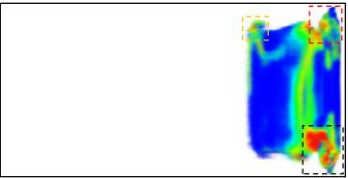
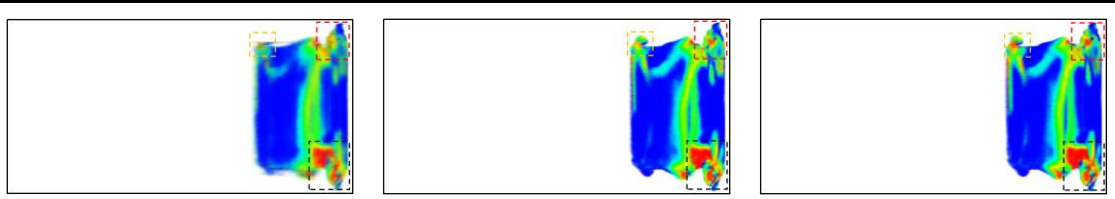
Ite	Results	281 iterations	563 iterations	1,126 iterations	2,817 iterations	5,633 iterations
0 th	$a=0$					
	stress=0					
	strain=0					
100 th	$a=3.5E+5$					
	stress=1.2E-4					
	strain=1.157					
1,000 th	$a=2.6E+6$					
	stress=473.6					
	strain=1.840					
2,500 th	$a=7.0E+5$					
	stress=473.6					
	strain=2.514					
5,000 th	$a=1.2E+7$					
	stress=473.6					
	strain=23.10					

Table 4 Enlarged images in the 5,000th iteration when simulating different iterations for the cube mapping on xOy surface.

Actual simulation	281 iterations	563 iterations
 <p>$a=1.2E+7m/s^2$ stress=473.6MPa strain=23.10</p>		
1,126 iterations	2,817 iterations	5,633 iterations



In the following step, the feature values of those cases whose feature dimension is 1 are drawn in the xOy coordinate in order⁴ as shown in Fig. 12, respectively. Interestingly, whatever the iteration is, the extracted features of each case can distribute on a smooth curve well which can further illustrate the manifold learning of the AVAE. Thus, it can be more inferred that the AVAE can extract features of the physical field well with few simulation iterations.

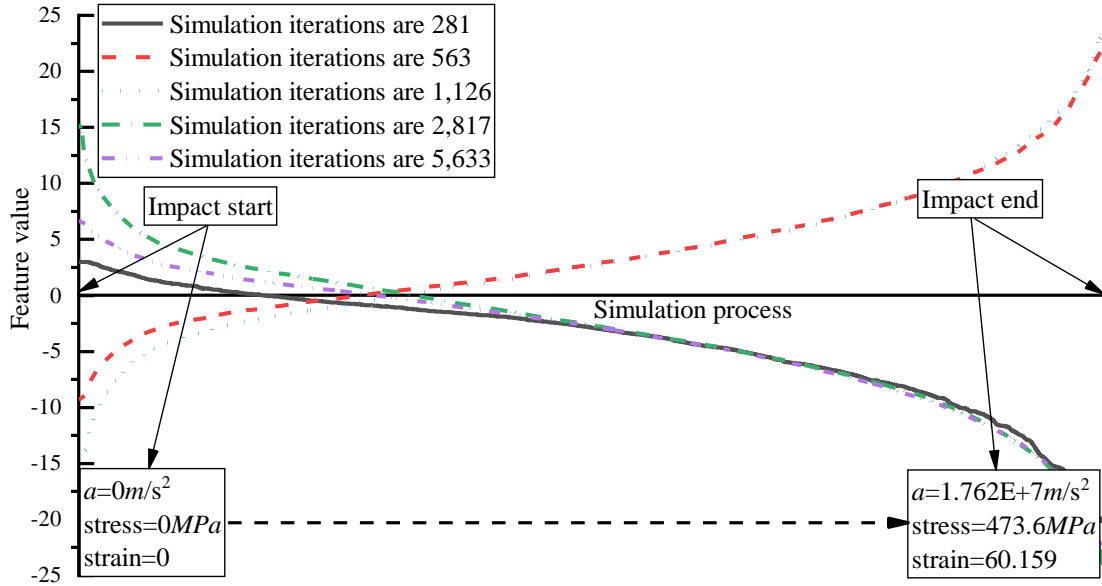


Fig. 12. The features of the physical field in the 1-dimensional manifold space for the cube mapping on xOy surface.

In summary, to easy observe the distribution of extracted features and be convenient to subsequent feature interpolation, the dimension of each feature is designed as 1. Moreover, comprehensive considering the display effect and this study is focused on the problems with few simulation iterations, the simulation of 563 iterations, namely 563 samples, is selected for follow-up researches. By the way,

⁴ The sampling process is from start to end of the collision process and iteration by iteration. Therefore, “in order” means that the samples are not disordered, and the decoding order of samples is the same as sampling order.

compared with the 22,000 samples in Ref. [28] and 6,055 samples in Ref. [29], the necessary samples of 563 are largely reduced and it makes this study more meaningful.

4.1.2. Reconstruction of the physical field.

In the ReConNN, after construct the mapping from images to objective functions by the CIC and generate more enough physical field images by the CWGAN, the curve of objective functions obtained from simulation will be interpolated. Then the new objective functions need to be matched with the generated images manually. Hence the new images can be interpolated into the initial simulation iterations. However, as mentioned in Section 1, the interpolation mode of the ReConNN has some shortcomings. Firstly, low-accuracy of the CNN influences the accuracy of the interpolation, and poor-diversity of the GAN might result in some interpolated iterations can't find suitable generated images. Moreover, it is impossible to guarantee that all structures of the generated physical fields are scientific and reasonable, so many computational resources will be consumed to generate meaningless images, and distinguishing available images from unavailable ones will be also inefficient. Finally, the matching work between interpolated objective functions and new physical field images is time-consuming and laborious.

Similar to the ReConNN, the Lagrange Interpolation (LI) is also employed to the final reconstruction. However, as for the EReConNN, the LI is no longer applied to the objective function values, but to the ordered 1-dimensional features of the physical field. Meanwhile, the generative model is also no longer the GAN, but the decoder of the AVAE. So while training the AVAE, the feature extraction model and generative model are trained simultaneously. The LI can be expressed by

$$f(x) = \sum_{i=1}^n y_i p_i(x), i = 1, 2, \dots, n \quad (33)$$

s.t.

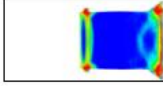
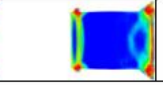
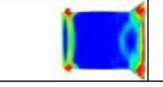
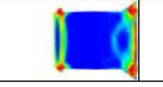
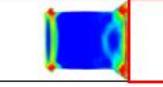
$$p_i = \prod_{j=1, j \neq i}^n \frac{x - x_j}{x_i - x_j} = \frac{(x - x_1)(x - x_2) \dots (x - x_n)}{(x_i - x_1) \dots (x_i - x_{i-1})(x_i - x_{i+1}) \dots (x_i - x_n)} \quad (34)$$

In this study, the interval of interpolation between adjacent collision iterations is

0.1, namely each adjacent iterations will be interpolated by 9 new values. The reconstructed results of interpolation and corresponding generated images for some iterations are shown in Table 5, where I_i means the i -th ($i=1, 2, \dots, 563$) iteration run by the real simulation; D_j ($j=1, 2, \dots, 9$) is j -th interpolated step; S is the abbreviate of the stress whose actual simulation iterations are set as 5,067 ($=563 \times 9$); D-S is the interpolated results of the stress between I_i and I_{i+1} ; and Error is the error of S and D-S. Furthermore, the parts marked with red are the actual iterations run by simulation, while others are the interpolated results. Two iteration processes during the collision are selected to be shown, the first (from I_7 to I_8) is the period of violent collision, another (from I_{324} to I_{325}) has been gradually converged. It can be inferred from Table 5 that through the decoder of the AVAE, the interpolated features are decoded well and orderly, and it is easily to guarantee the interpolated objective functions and generated images match well. Moreover, the errors between interpolated and actual simulation results are less than 10^{-4} which satisfies sufficiently.

Table 5 The reconstruction of the strong-nonlinear physical field of the collision problem for the cube mapping on xOy surface.

Legend		I_7	D_1	D_2	D_3	D_4
Image	<div><div>S_Mises SNEG, (fraction = -1.0) (Avg: 75%)</div><div><div></div><div></div><div></div><div></div><div></div><div></div><div></div><div></div><div></div><div></div><div></div><div></div><div></div><div></div><div></div><div></div><div></div><div></div><div></div><div></div><div></div><div></div><div></div><div></div><div></div><div></div><div></div><div></div><div></div><div></div><div></div><div></div><div></div><div></div><div></div><div></div><div></div><div></div><div></div><div></div><div></div><div></div><div></div><div></div><div></div><div></div><div></div><div></div><div></div><div></div><div></div><div></div><div></div><div></div><div></div><div></div><div></div><div></div><div></div><div></div><div></div><div></div><div></div><div></div><div></div><div></div><div></div><div></div><div></div><div></div><div></div><div></div><div></div><div></div><div></div><div></div><div></div><div></div><div></div><div></div><div></div><div></div><div></div><div></div><div></div><div></div><div></div><div></div><div></div><div></div><div></div><div></div><div></div><div></div><div></div><div></div><div></div><div></div><div></div><div></div><div></div><div></div><div></div><div></div><div></div><div></div><div></div><div></div><div></div><div></div><div></div><div></div><div></div><div></div><div></div><div></div><div></div><div></div><div></div><div></div><div></div><div></div><div></div><div></div><div></div><div></div><div></div><div></div><div></div><div></div><div></div><div></div><div></div><div></div><div></div><div></div><div></div><div></div><div></div><div></div><div></div><div></div><div></div><div></div><div></div><div></div><div></div><div></div><div></div><div></div><div></div><div></div><div></div><div></div><div></div><div></div><div></div><div></div><div></div><div></div><div></div><div></div><div></div><div></div><div></div><div></div><div></div><div></div><div></div><div></div><div></div><div></div><div></div><div></div><div></div><div></div><div></div><div></div><div></div><div></div><div></div><div></div><div></div><div></div><div></div><div></div><div></div><div></div><div></div><div></div><div></div><div></div><div></div><div></div><div></div><div></div><div></div><div></div><div></div><div></div><div></div><div></div><div></div><div></div><div></div><div></div><div></div><div></div><div></div><div></div><div></div><div></div><div></div><div></div><div></div><div></div><div></div><div></div><div></div><div></div><div></div><div></div><div></div><div></div><div></div><div></div><div></div><div></div><div></div><div></div><div></div><div></div><div></div><div></div><div></div><div></div><div></div><div></div><div></div><div></div><div></div><div></div><div></div><div></div><div></div><div></div><div></div><div></div><div></div><div></div><div></div><div></div><div></div><div></div><div></div><div></div><div></div><div></div><div></div><div></div><div></div><div></div><div></div><div></div><div></div><div></div><div></div><div></div><div></div><div></div><div></div><div></div><div></div><div></div><div></div><div></div><div></div><div></div><div></div><div></div><div></div><div></div><div></div><div></div><div></div><div></div><div></div><div></div><div></div><div></div><div></div><div></div><div></div><div></div><div></div><div></div><div></div><div></div><div></div><div></div><div></div><div></div><div></div><div></div><div></div><div></div><div></div><div></div><div></div><div></div><div></div><div></div><div></div><div></div><div></div><div></div><div></div><div></div><div></div><div></div><div></div><div></div><div></div><div></div><div></div><div></div><div></div><div></div><div></div><div></div><div></div><div></div><div></div><div></div><div></div><div></div><div></div><div></div><div></div><div></div><div></div><div></div><div></div><div></div><div></div><div></div><div></div><div></div><div></div><div></div><div></div><div></div><div></div><div></div><div></div><div></div><div></div><div></div><div></div><div></div><div></div><div></div><div></div><div></div><div></div><div></div><div></div><div></div><div></div><div></div><div></div><div></div><div></div><div></div><div></div><div></div><div></div><div></div><div></div><div></div><div></div><div></div><div></div><div></div><div></div><div></div><div></div><div></div><div></div><div></div><div></div><div></div><div></div><div></div><div></div><div></div><div></div><div></div><div></div><div></div><div></div><div></div><div></div><div></div><div></div><div></div><div></div><div></div><div></div><div></div><div></div><div></div><div></div><div></div><div></div><div></div><div></div><div></div><div></div><div></div><div></div><div></div><div></div><div></div><div></div><div></div><div></div><div></div><div></div><div></div><div></div><div></div><div></div><div></div><div></div><div></div><div></div><div></div><div></div><div></div><div></div><div></div><div></div><div></div><div></div><div></div><div></div><div></div><div></div><div></div><div></div><div></div><div></div><div></div><div></div><div></div><div></div><div></div><div></div><div></div><div></div><div></div><div></div><div></div><div></div><div></div><div></div><div></div><div></div><div></div><div></div><div></div><div></div><div></div><div></div><div></div><div></div><div></div><div></div><div></div><div></div><div></div><div></div><div></div><div></div><div></div><div></div><div></div><div></div><div></div><div></div><div></div><div></div><div></div><div></div><div></div><div></div><div></div><div></div><div></div><div></div><div></div><div></div><div></div><div></div><div></div><div></div><div></div><div></div><div></div><div></div><div></div><div></div><div></div><div></div><div></div><div></div><div></div><div></div><div></div><div></div><div></div><div></div><div></div><div></div><div></div><div></div><div></div><div></div><div></div><div></div><div></div><div></div><div></div><div></div><div></div><div></div><div></div><div></div><div></div><div></div><div></div><div></div><div></div><div></div><div></div><div></div><div></div><div></div><div></div><div></div><div></div><div></div><div></div><div></div><div></div><div></div><div></div><div></div><div></div><div></div><div></div><div></div><div></div><div></div><div></div><div></div><div></div><div></div><div></div><div></div><div></div><div></div><div></div><div></div><div></div><div></div><div></div><div></div><div></div><div></div><div></div><div></div><div></div><div></div><div></div><div></div><div></div><div></div><div></div><div></div><div></div><div></div><div></div><div></div><div></div><div></div><div></div><div></div><div></div><div></div><div></div><div></div><div></div><div></div><div></div><div></div><div></div><div></div><div></div><div></div><div></div><div></div><div></div><div></div><div></div><div></div><div></div><div></div><div></div><div></div><div></div><div></div><div></div><div></div><div></div><div></div><div></div><div></div><div></div><div></div><div></div><div></div><div></div><div></div><div></div><div></div><div></div><div></div><div></div><div></div><div></div><div></div><div></div><div></div><div></div><div></div><div></div><div></div><div></div><div></div><div></div><div></div><div></div><div></div><div></div><div></div><div></div><div></div><div></div><div></div><div></div><div></div><div></div><div></div><div></div><div></div><div></div><div></div><div></div><div></div><div></div><div></div><div></div><div></div><div></div><div></div><div></div><div></div><div></div><div></div><div></div><div></div><div></div><div></div><div></div><div></div><div></div><div></div><div></div><div></div><div></div><div></div><div></div><div></div><div></div><div></div><div></div><div></div><div></div><div></div><div></div><div></div><div></div><div></div><div></div><div></div><div></div><div></div><div></div><div></div><div></div><div></div><div></div><div></div><div></div><div></div><div></div><div></div><div></div><div></div><div></div><div></div><div></div><div></div><div></div><div></div><div></div><div></div><div></div><div></div><div></div><div></div><div></div><div></div><div></div><div></div><div></div><div></div><div></div><div></div><div></div><div></div><div></div><div></div><div></div><div></div><div></div><div></div><div></div><div></div><div></div><div></div><div></div><div></div><div></div><div></div><div></div><div></div><div></div><div></div><div></div><div></div><div></div><div></div><div></div><div></div><div></div><div></div><div></div><div></div><div></div><div></div><div></div><div></div><div></div><div></div><div></div><div></div><div></div><div></div><div></div><div></div><div></div><div></div><div></div><div></div><div></div><div></div><div></div><div></div><div></div><div></div><div></div><div></div><div></div><div></div><div></div><div></div><div></div><div></div><div></div><div></div><div></div><div></div><div></div><div></div><div></div><div></div><div></div><div></div><div></div><div></div><div></div><div></div><div></div><div></div><div></div><div></div><div></div><div></div><div></div><div></div><div></div><div></div><div></div><div></div><div></div><div></div><div></div><div></div><div></div><div></div><div></div><div></div><div></div><div></div><div></div><div></div><div></div><div></div><div></div><div></div><div></div><div></div><div></div><div></div><div></div><div></div><div></div><div></div><div></div><div></div><div></div><div></div><div></div><div></div><div></div><div></div><div></div><div></div><div></div><div></div><div></div><div></div><div></div><div></div><div></div><div></div><div></div><div></div><div></div><div></div><div></div><div></div><div></div><div></div><div></div><div></div><div></div><div></div><div></div><div></div><div></div><div></div><div></div><div></div><div></div><div></div><div></div><div></div><div></div><div></div><div></div><div></div><div></div><div></div><div></div><div></div><div></div><div></div><div></div><div></div><div></div><div></div><div></div><div></div><div></div><div></div><div></div><div></div><div></div><div></div><div></div><div></div><div></div><div></div><div></div><div></div><div></div><div></div><div></div><div></div><div></div><div></div><div></div><div></div><div></div><div></div><div></div><div></div><div></div><div></div><div></div><div></div><div></div><div></div><div></div><div></div><div></div><div></div><div></div><div></div><div></div><div></div><div></div><div></div><div></div><div></div><div></div><div></div><div></div><div></div><div></div><div></div><div></div><div></div><div></div><div></div><div></div><div></div><div></div><div></div><div></div><div></div><div></div><div></div><div></div><div></div><div></div><div></div><div></div><div></div><div></div><div></div><div></div><div></div><div></div><div></div><div></div><div></div><div></div><div></div><div></div><div></div><div></div><div></div><div></div><div></div><div></div><div></div><div></div><div></div><div></div><div></div><div></div><div></div><div></div><div></div><div></div><div></div><div></div><div></div><div></div><div></div><div></div><div></div><div></div><div></div><div></div><div></div><div></div><div></div><div></div><div></div><div></div><div></div><div></div><div></div><div></div><div></div><div></div><div></div><div></div><div></div><div></div><div></div><div></div><div></div><div></div><div></div><div></div><div></div><div></div><div></div><div></div><div></div><div></div><div></div><div></div><div></div><div></div><div></div><div></div><div></div><div></div><div></div><div></div><div></div><div></div><div></div><div></div><div></div><div></div><div></div><div></div><div></div><div></div><div></div><div></div><div></div><div></div><div></div><div></div><div></div><div></div><div></div><div></div><div></div><div></div><div></div><div></div><div></div><div></div><div></div><div></div><div></div><div></div><div></div><div></div><div></div><div></div><div></div><div></div><div></div><div></div><div></div><div></div><div></div><div></div><div></div><div></div><div></div><div></div><div></div><div></div><div></div><div></div><div></div><div></div><div></div><div></div><div></div><div></div><div></div><div></div><div></div><div></div><div></div><div></div><div></div><div></div><div></div><div></div><div></div><div></div><div></div><div></div><div></div><div></div><div></div><div></div><div></div><div></div><div></div><div></div><div></div><div></div><div></div><div></div><div></div><div></div><div></div><div></div><div></div><div></div><div></div><div></div><div></div><div></div><div></div><div></div><div></div><div></div><div></div><div></div><div></div><div></div><div></div><div></div><div></div><div></div><div></div><div></div><div></div><div></div><div></div><div></div><div></div><div></div><div></div><div></div><div></div><div></div><div></div><div></div><div></div><div></div><div></div><div></div><div></div><div></div><div></div><div></div><div></div><div></div><div></div><div></div><div></div><div></div><div></div><div></div><div></div><div></div><div></div><div></div><div></div><div></div><div></div><div></div><div></div><div></div><div></div><div></div><div></div><div></div><div></div><div></div><div></div><div></div><div></div><div></div><div></div><div></div><div></div><div></div><div></div><div></div><div></div><div></div><div></div><div></div><div></div><div></div><div></div><div></div><div></div><div></div><div></div><div></div><div></div><div></div><div></div><div></div><div></div><div></div><div></div><div></div><div></div><div></div><div></div><div></div><div></div><div></div><div></div><div></div><div></div><div></div><div></div><div></div><div></div><div></div><div></div><div></div><div></div><div></div><div></div><div></div><div></div><div></div><div></div><div></div><div></div><div></div><div></div><div></div><div></div><div></div><div></div><div></div><div></div><div></div><div></div><div></div><div></div><div></div><div></div><div></div><div></div><div></div><div></div><div></div><div></div><div></div><div></div><div></div><div></div><div></div><div></div><div></div><div></div><div></div><div></div><div></div><div></div><div></div><div></div><div></div><div></div><div></div><div></div><div></div><div></div><div></div><div></div><div></div><div></div><div></div><div></div><div></div><div></div><div></div><div></div><div></div><div></div><div></div><div></div><div></div><div></div><div></div><div></div><div></div><div></div><div></div><div></div><div></div><div></div><div></div><div></div><div></div><div></div><div></div><div></div><div></div><div></div><div></div><div></div><div></div><div></div><div></div><div></div><div></div><div></div><div></div><div></div><div></div><div></div><div></div><div></div><div></div><div></div><div></div><div></div><div></div><div></div><div></div><div></div><div></div><div></div><div></div><div></div><div></div><div></div><div></div><div></div><div></div><div></div><div></div><div></div><div></div><div></div><div></div><div></div><div></div><div></div><div></div><div></div><div></div><div></div><div></div><div></div><div></div><div></div><div></div><div></div><div></div><div></div><div></div><div></div><div></div><div></div><div></div><div></div><div></div><div></div><div></div><div></div><div></div><div></div><div></div><div></div><div></div><div></div><div></div><div></div><div></div><div></div><div></div><div></div><div></div><div></div><div></div><div></div><div></div><div></div><div></div><div></div><div></div><div></div><div></div><div></div><div></div><div></div><div></div><div></div><div></div><div></div><div></div></div></div>					

Feature	3.924	3.926	3.929	3.931	3.934
S	473.602	473.603	473.605	473.608	473.611
D-S	--	473.603	473.605	473.608	473.611
Error	--	0.00%	0.00%	0.00%	0.00%
	D ₅	D ₆	D ₇	D ₈	D ₉
					I₃₂₅
Image					
Feature	3.936	3.939	3.941	3.944	3.946
S	473.615	473.619	473.622	473.625	473.627
D-S	473.615	473.619	473.622	473.625	473.627
Error	0.00%	0.00%	0.00%	0.00%	0.00%

4.1.3. Visualization Enhancement of the physical field.

As mentioned before, although the reconstructed result of the physical field can represent the overall structure, it lacks some detail features. It is necessary to enhance the visualization results.

The decoded images are used as the inputs to the CGAN, while corresponding simulated images are the generative objectives. In order to judge the quality of the enhanced images, peak signal-to-noise ratio (PSNR) [47] and structural similarity (SSIM) [48] are employed and calculated by Eqs. (35) - (36) and Eq. (37), respectively. The PSNR is an engineering term for the ratio between the maximum possible power of a signal and the power of corrupting noise that affects the fidelity of its representation. When given a noise-free $m \times n$ monochrome image I and its noisy approximation K , the Eq. (23) can be changed as

$$MSE = \frac{1}{nm} \sum_{i=0}^{n-1} \sum_{j=0}^{m-1} [I(i, j) - K(i, j)]^2 \quad (35)$$

The PSNR is defined as

$$PSNR = 10 \cdot \log_{10} \left(\frac{MAX^2}{MSE} \right) = 20 \cdot \log_{10}(MAX) - 10 \cdot \log_{10}(MSE) \quad (\text{dB}) \quad (36)$$

where MAX is the maximum possible pixel value of the image. Usually it is 255.

As for the SSIM, it is used for measuring the similarity between two images. The SSIM is designed to improve on traditional methods such as PSNR and MSE. It is a value between 0 and 1, and the larger the SSIM, the better the image quality. It is

calculated by

$$SSIM = \frac{(2\mu_I\mu_K + c_1)(2\sigma_{IK} + c_2)}{(\mu_I^2 + \mu_K^2 + c_1)(\sigma_I^2 + \sigma_K^2 + c_2)} \quad (37)$$

that

$$c_1 = (k_1 L)^2, c_2 = (k_2 L)^2 \quad (38)$$

where μ_I and μ_K are the pixel average of image I and K , respectively; σ_I^2 and σ_K^2 are the pixel variance of image I and K , respectively; σ_{IK} is the covariance of I and K ; c_1 and c_2 are to stabilize the division with weak denominator; and L is the dynamic range of the pixel-values. $L=255$, $k_1=0.01$ and $k_2=0.03$ by default.

The enhanced results are shown in Fig. 13. It can be seen that the CGAN improves the decoded images satisfactorily, especially in those marked areas, and the representation of detailed features is also improved greatly. As for the PSNR and SSIM, empirically, if the PSNR and SSIM are larger than 20 and 0.9, respectively, the results are acceptable.

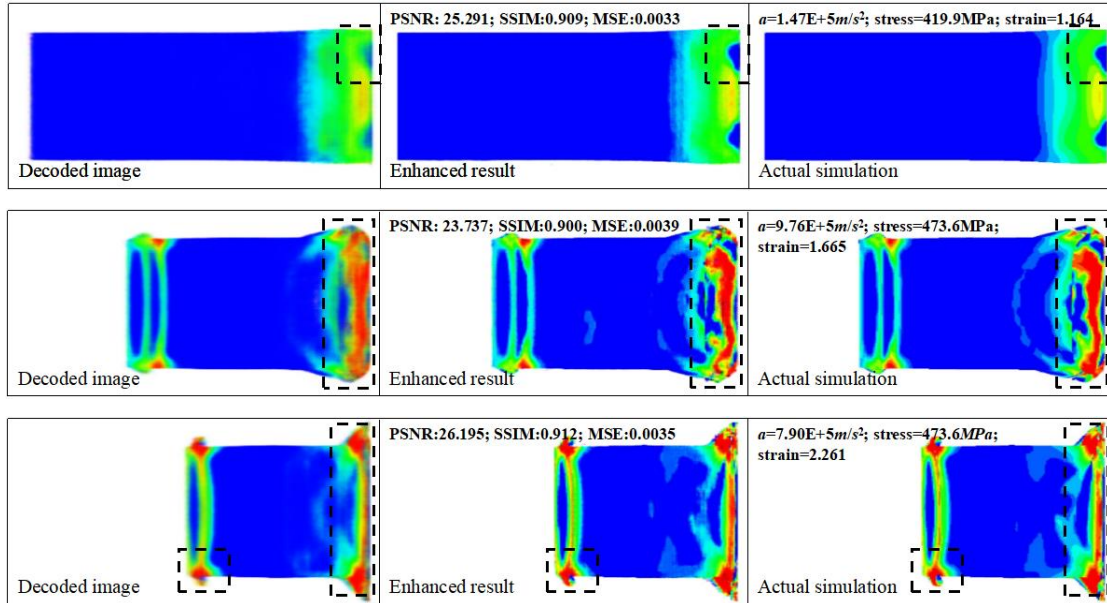


Fig. 13. Enhanced results of the reconstruction for the cube mapping on xOy surface.

4.2. The reconstruction of the mapping on the $x=y=z$ surface

In this section, the reconstruction of the collision problem will be constructed on the mapping surface of $x=y=z$. From this surface, the 3D changes and folding of the

body during the collision can be better observed and obtained.

4.2.1. Feature extraction of the physical field.

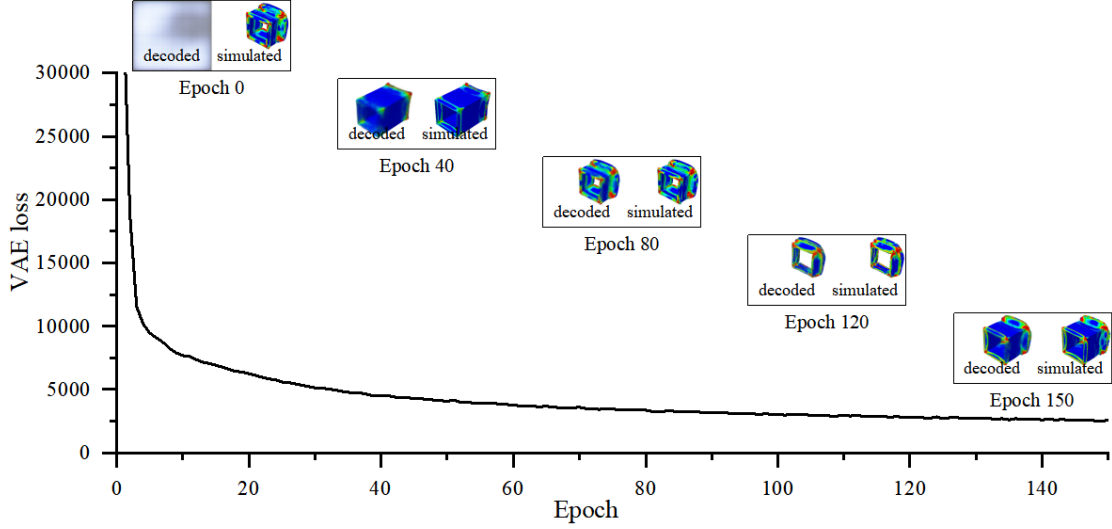


Fig. 14. The feature extraction process of the physical field by using the AVAE for the cube mapping on $x=y=z$ surface.

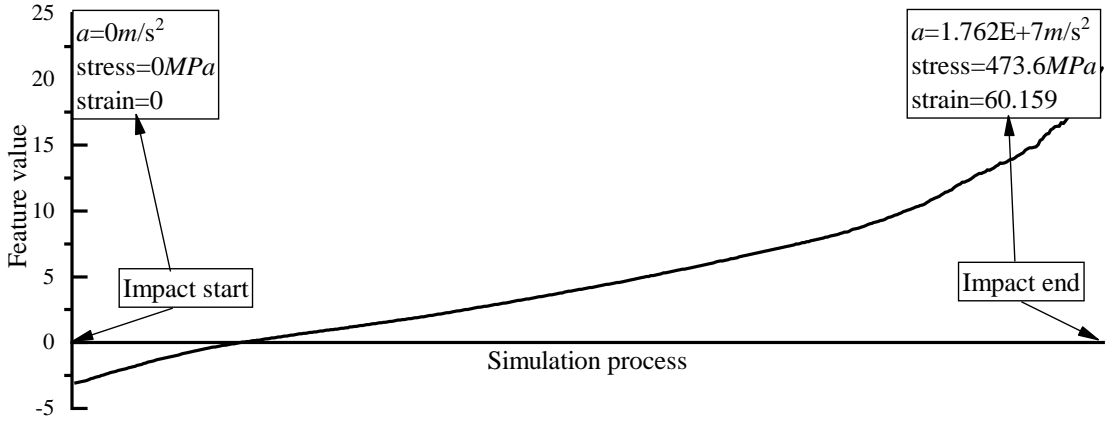



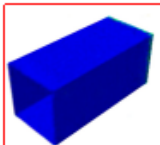
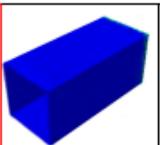
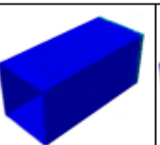
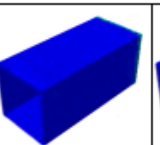
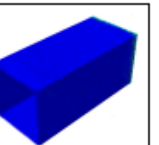
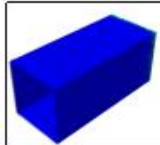
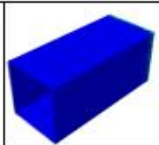
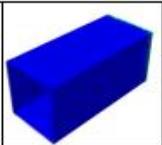
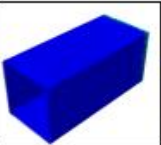
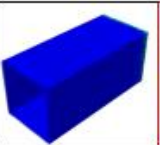
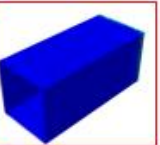

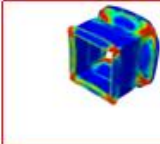
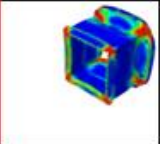
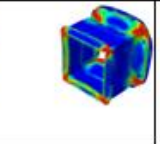
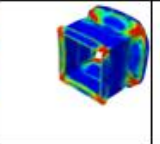
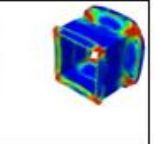
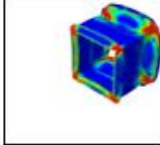
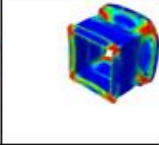
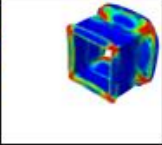
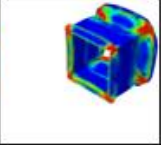
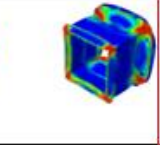
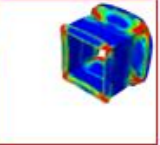
Fig. 15. The manifold distribution of the physical field in 1-dimensional space for the cube mapping on $x=y=z$ surface.

Firstly, the AVAE is applied to extract the physical field features. As mentioned in Section 4.1.1, the final simulation iterations are selected as 563, so the sample size is 563. As shown in Fig. 14, after training 150 epochs, the decoded images by the AVAE can basically present the overall characteristics of the physical field. Furthermore, as shown in Fig. 15, through the manifold learning, the physical field well maps from high-dimensional to 1-dimensional spaces.

4.2.2. Reconstruction of the physical field.

As the same as the reconstruction of the mapping on the xOy surface, the reconstructions from 7th to 8th iterations and from 324th to 325th iterations are shown in Table 6, respectively. Compared with the actual simulation process, the simulation iterations of the physical field increase 9 times easily, and the added steps have high enough resolutions and many enough detailed features.

Table 6 The reconstruction of the strong-nonlinear physical field of the collision problem for the cube mapping on $x=y=z$ surface.

Legend		I_7	D_1	D_2	D_3	D_4	
Image	<div>S, Mises SNEG, (fraction = -1.0) (Avg: 75%) </div>						
Feature		-7.410	-7.379	-7.348	-7.317	-7.287	
S		404.614	404.972	405.318	405.650	405.964	
D-S		--	404.959	405.279	405.580	405.864	
Error		--	0.00%	0.01%	0.02%	0.02%	
Legend		D_5	D_6	D_7	D_8	D_9	I_8
Image							
Feature	-7.257	-7.229	-7.201	-7.174	-7.149	-7.125	
S	406.256	406.536	406.797	407.037	407.261	407.474	
D-S	406.137	406.403	406.665	406.928	407.196	--	
Error	0.03%	0.03%	0.03%	0.03%	0.02%	--	
Legend		I_{324}	D_1	D_2	D_3	D_4	
Image	<div>S, Mises SNEG, (fraction = -1.0) (Avg: 75%) </div>						
Feature		3.924	3.926	3.929	3.931	3.934	
S		473.602	473.603	473.605	473.608	473.611	
D-S		--	473.603	473.605	473.608	473.611	
Error		--	0.00%	0.00%	0.00%	0.00%	
Legend		D_5	D_6	D_7	D_8	D_9	I_{325}
Image							

Feature	3.936	3.939	3.941	3.944	3.946	3.949
S	473.615	473.619	473.622	473.625	473.627	473.627
D-S	473.615	473.619	473.622	473.625	473.627	--
Error	0.00%	0.00%	0.00%	0.00%	0.00%	--

4.2.3. Visualization enhancement of the physical field.

After training 150 epochs, the enhanced results are shown in Fig. 16. Compared with the mapping on xOy surface, the PSNR and SSIM are litter worse due to containing more detailed features from the 3D view, while the folding is better shown. Comprehensively, the enhanced results are satisfied and acceptable.

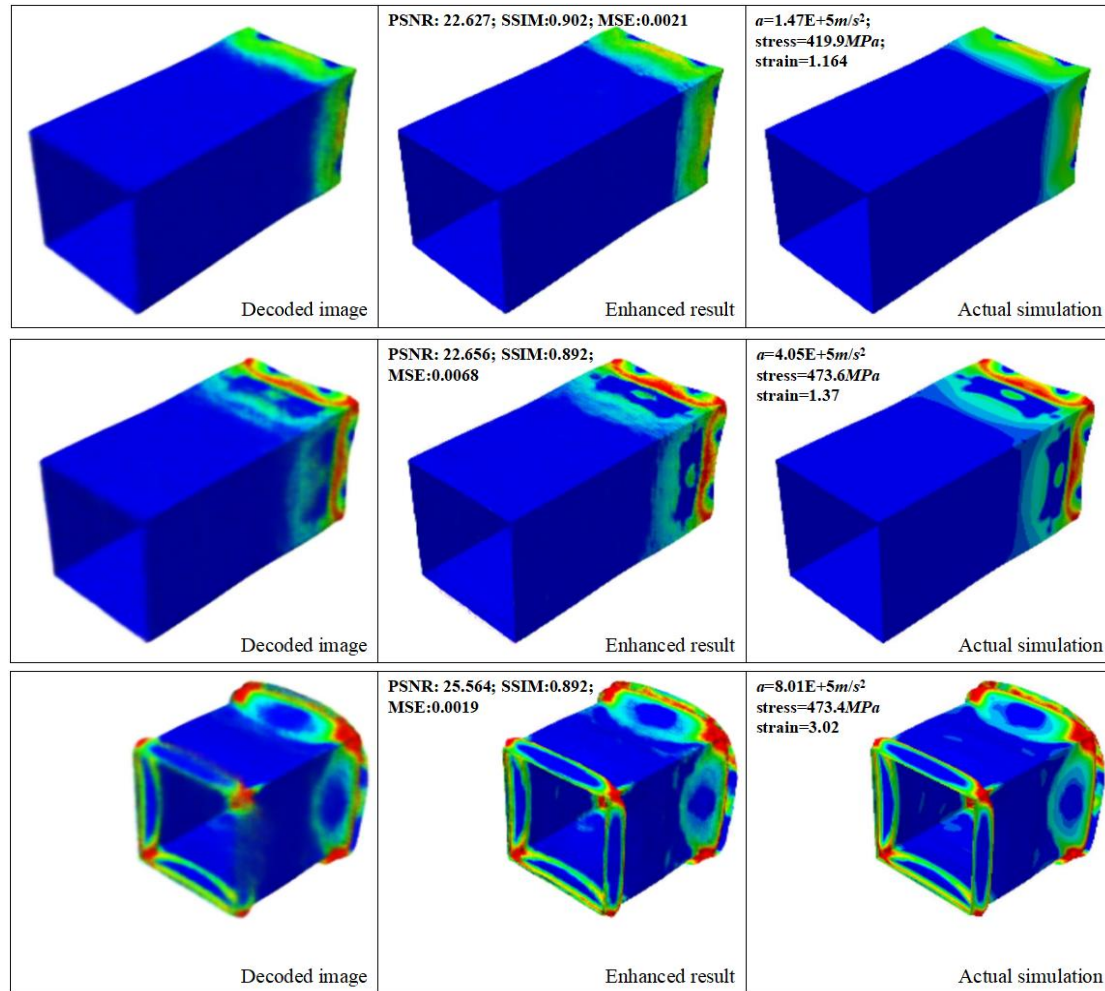


Fig. 16. Enhanced results of the reconstruction for the cube mapping on $x=y=z$ surface.

5. Experiments

Recently, the structure crashworthiness of vehicles has attracted increasingly attentions [49-51]. The thin-walled metal structure is considered as a promising

energy absorber for its efficient energy absorption performance [52]. In this section, the collision of a combined five-cell thin-walled structure used in high speed train [52] is employed and simulated. Then the collision process is reconstructed by using limited simulation iterations. Consequently, a full scale collision experiment is done to validate the reconstructed results.

5.1. Physical model

5.1.1. Combined five-cell structure.

As shown in Fig. 17, the combined multi-cell thin-walled aluminum structure is installed in the front end of certain high speed trains. The units of the sizes in Fig. 17 are *mm*, and the thickness is designed as *5mm*. The material structure is designed as Al alloy 6,008 as shown in Table 7. It contains one octagonal and four hexagonal tubes.

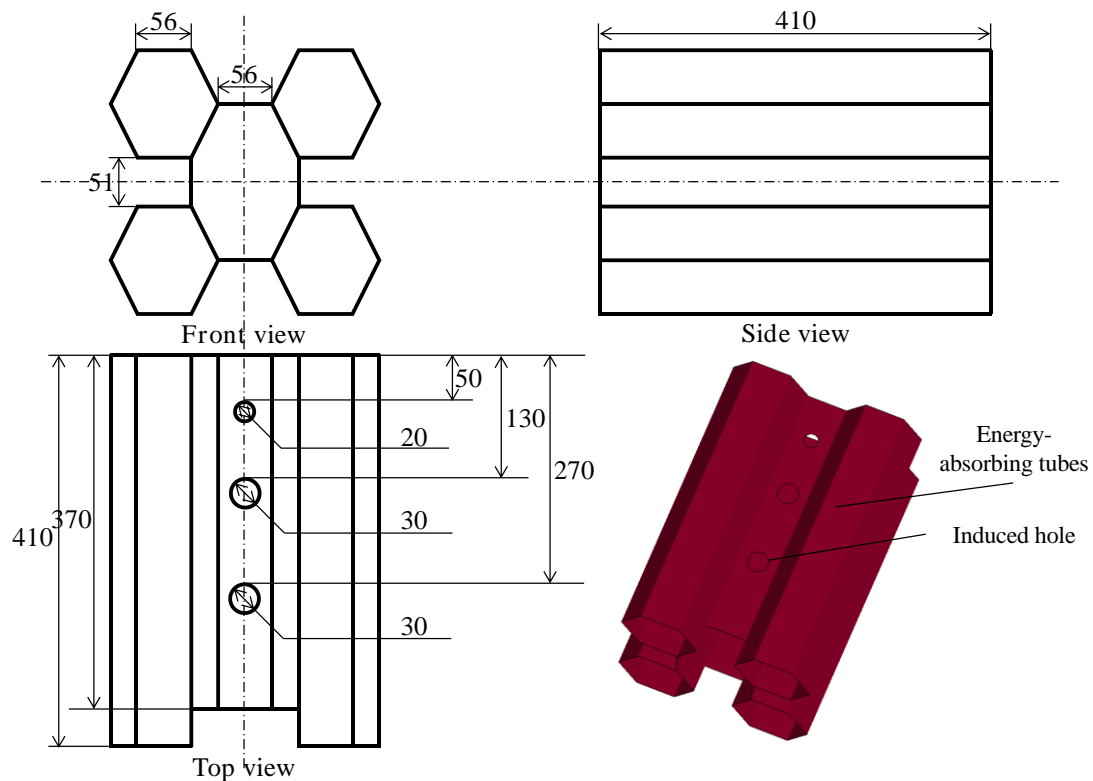


Fig. 17. The CAD model of the combined five-cell.

Table 7 The material parameters of the Al alloy 6,008.

Parameter	Value
Young's modulus (<i>MPa</i>)	72,000

Poisson's ratio	0.33	
Yield stress (<i>MPa</i>)	131.82	
Density (<i>t/mm</i> ³)	2.7×10 ⁻⁹	
Hardening curve	Yield stress (<i>MPa</i>)	Plastic deformation
	131.8	0
	140.0	0.0023
	149.4	0.0067
	162.3	0.0153
	171.2	0.0232
	178.3	0.0314
	183.7	0.0406
	187.4	0.0503
	189.8	0.0601
	190.6	0.0648
	191.0	0.0658

5.1.2. The simulation model of the collision.

As shown in Fig. 18, the collision model is composed of collision trolley, energy-absorbing structure and rigid tracks. To keep consistent with actual conditions, a $9.81m/s^2$ gravity acceleration is adopted to the entire system. The frictional coefficients for static and dynamic conditions are designed as 0.3 and 0.1, respectively. The 2,000kg trolley collides as an initial velocity of $15.510m/s$.

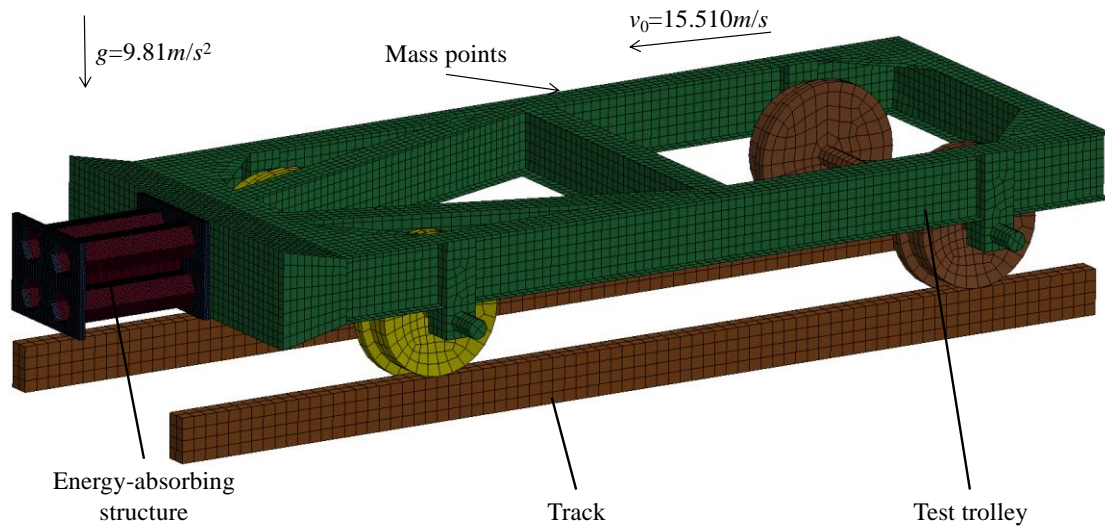


Fig. 18. The FE model and simulation conditions.

5.2. Reconstruction by using the EReConNN

In this section, the collision process mapping on the top view is reconstructed,

and 100 iterations are simulated to obtain training samples.

5.2.1. Feature extraction of the physical field.

The manifold distribution of the physical field in 1-dimensional space are represented in Figs. 19. It can be found that the AVAE well maps the physical field of the combined five-cell from high-dimensional to 1-dimensional manifold spaces.

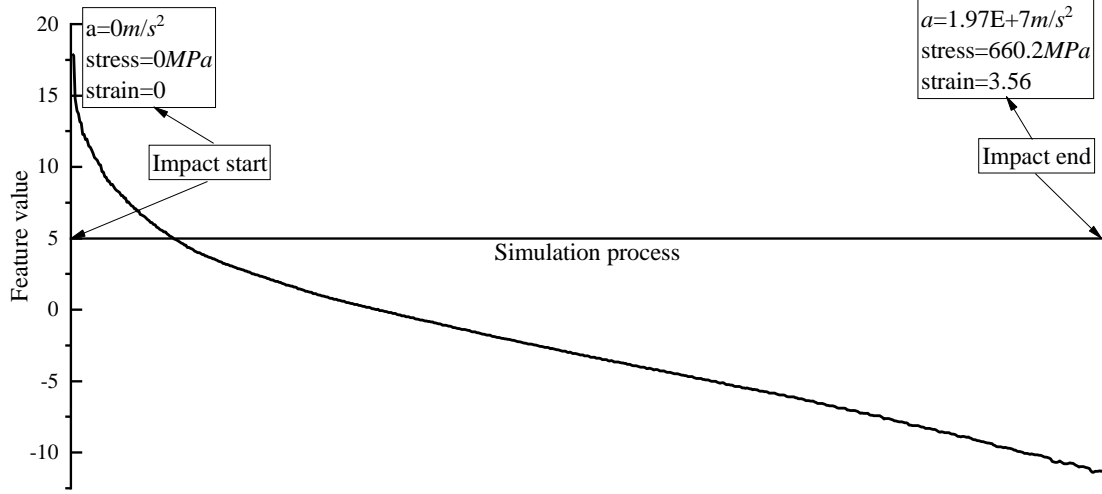


Fig. 19. The manifold distribution in 1-dimensional space for the combined five-cell.

5.2.2. Reconstruction of the physical field.

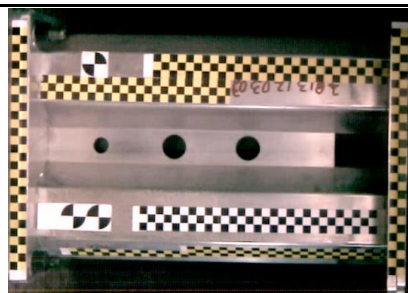
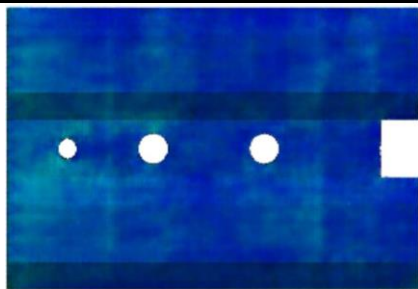
The collision process spends 40ms, and the collision images in 0ms, 0.4ms, 0.8ms, ..., 40ms in simulation are saved, namely 2,500 frames per second. As shown in Table 8, following the reconstruction thought in Section 4 and taking 0.04ms as the interpolation step, 9 times iterations of the initial simulation are obtained, namely 25,000 frames per second. Furthermore, an experiment is done to evaluated the reconstruction results. The collision process of the experiment is captured by a high speed camera with a frequency of 5,000 frames per second.

It can be seen that the reconstructed collision process is consistent well with the experiment. The tubes buckle symmetrically along the central axis. Moreover, 5 times of sampling frequency are well obtained compared with the high speed camera, which can help us reduce the computational and equipment costs effectively.

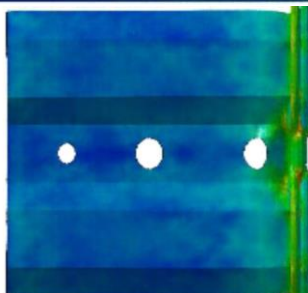
Table 8 Comparisons of collision series between reconstructed and experimental.

Time	Reconstruction	Experiment
------	----------------	------------

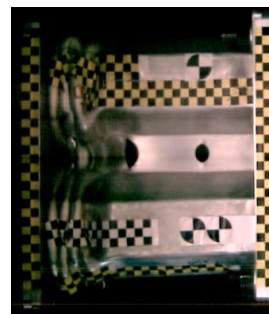
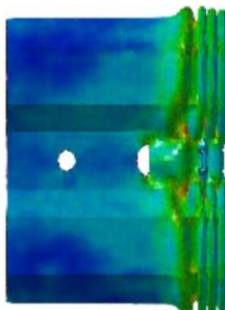
0.6ms



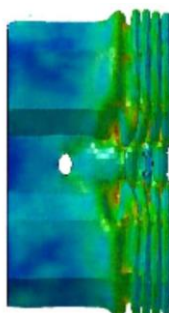
8.2ms



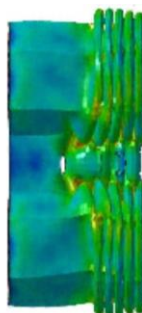
16.2ms



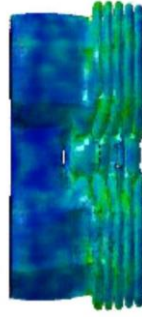
24.2ms



32.2ms



40.2ms



Conclusions

In this study, an enhanced ReConNN, namely EReConNN is developed to solve a strong-nonlinear transient collision case. Simultaneously, the EReConNN addresses some shortcomings of the existing ReConNN. Its advantages in this study can be summarized as follows.

- i. The proposed EReConNN is successfully applied to a strong-nonlinear transient case, a collision problem;
- ii. The reasons why the GAN preforms badly in the strong-nonlinear case while the AE can outperform are analyzed detailedly;
- iii. The integrated mode of the CNN and GAN is replaced by an AVAE, which completes the feature extract and image generation simultaneously. It avoids the disadvantage of poor-diversity of the CWGAN in the ReConNN;
- iv. The KL algorithm is no longer only used to the objective functions, but to the objective functions and extracted ordered features, which solves the low-accuracy disadvantage of the CIC in the ReConNN efficiently;
- v. After generating new design images, the CGAN is employed to improve the generated images. This makes the reconstructive results have more meaningful features and more similar to the actual simulation results;
- vi. Subsequently, a strong-nonlinear transient collision problem is calculated by the EReConNN successfully, which is very hard for the ReConNN;
- vii. Finally, the collision process of a thin-walled metal structure is reconstructed and experimented. The comparison results present that the proposed EReConNN can well reduce the computational and equipment costs effectively.

Acknowledgments

This work has been supported by Project of the Key Program of National Natural Science Foundation of China under the Grant Numbers 11572120 and 51621004, Key Projects of the Research Foundation of Education Bureau of Hunan Province (17A224).

Reference

- [1]. Oishi A, Yagawa G. Computational mechanics enhanced by deep learning. *Computer Methods in Applied Mechanics and Engineering*. 2017;327:327-51.
- [2]. Cheng Z, Wang H. How to control the crack to propagate along the specified path feasibly? *Computer Methods in Applied Mechanics and Engineering*. 2018;336:554-77.
- [3]. Papadopoulos V, Soimiris G, Giovanis DG, Papadrakakis M. A neural network-based surrogate model for carbon nanotubes with geometric nonlinearities. *Computer Methods in Applied Mechanics and Engineering*. 2018;328:411-30.
- [4]. Wang H, Li GY, Li E. Time-based metamodeling technique for vehicle crashworthiness optimization. *Computer Methods in Applied Mechanics & Engineering*. 2010;199(37):2497-509.
- [5]. White DA, Arrighi WJ, Kudo J, Watts SE. Multiscale topology optimization using neural network surrogate models. *Computer Methods in Applied Mechanics and Engineering*. 2019;346:1118-35.
- [6]. Lin C-Y, Lin S-H. Artificial neural network based hole image interpretation techniques for integrated topology and shape optimization. *Computer methods in applied mechanics and engineering*. 2005;194(36-38):3817-37.
- [7]. Sheikholeslami M, Gerdroodbary MB, Moradi R, Shafee A, Li Z. Application of Neural Network for estimation of heat transfer treatment of Al₂O₃-H₂O nanofluid through a channel. *Computer Methods in Applied Mechanics and Engineering*. 2019;344:1-12.
- [8]. Cz  B, Woodbury KA, Gr f G. Inverse identification of temperature-dependent volumetric heat capacity by neural networks. *International Journal of Thermophysics*. 2013;34(2):284-305.
- [9]. Li X, Liu Z, Cui S, Luo C, Li C, Zhuang Z. Predicting the effective mechanical property of heterogeneous materials by image based modeling and deep learning. *Computer Methods in Applied Mechanics and Engineering*. 2019.
- [10]. Ootao Y KR, Tanigawa Y, et al. Optimization of material composition of nonhomogeneous hollow sphere for thermal stress relaxation making use of neural network. *Computer methods in applied mechanics and engineering*. 1999;180(1-2): 185-201.
- [11]. Wu J-L, Sun R, Laizet S, Xiao H. Representation of stress tensor perturbations with application in machine-learning-assisted turbulence modeling. *Computer Methods in Applied Mechanics and Engineering*. 2019;346:707-26.
- [12]. Kuan Y, Lien H, editors. *The integration of the neural network and computational fluid dynamics for the heatsink design*. International Symposium on Neural Networks; 2005: Springer.
- [13]. Qi Y, Lu J, Scardovelli R, Zaleski S, Tryggvason G. Computing curvature for volume of fluid methods using machine learning. *Journal of Computational Physics*. 2019;377:155-61.

- [14]. Poloni C, Giurgevich A, Onesti L, Pediroda V. Hybridization of a multi-objective genetic algorithm, a neural network and a classical optimizer for a complex design problem in fluid dynamics. *Computer Methods in Applied Mechanics & Engineering*. 2000;186(2):403-20.
- [15]. Lin Q, Hong J, Liu Z, Li B, Wang J. Investigation into the topology optimization for conductive heat transfer based on deep learning approach. *International Communications in Heat and Mass Transfer*. 2018;97:103-9.
- [16]. Sosnovik I, Oseledets I, Sosnovik I, Oseledets I. Neural networks for topology optimization. 2017.
- [17]. Yu Y, Hur T, Jung J, Jang IG. Deep learning for determining a near-optimal topological design without any iteration. *Structural and Multidisciplinary Optimization*. 2018:1-13.
- [18]. Banga S, Gehani H, Bhilare S, Patel S, Kara L. 3D Topology Optimization using Convolutional Neural Networks. arXiv preprint arXiv:180807440. 2018.
- [19]. Fan Z, Wu Y, Lu J, Li W. Automatic pavement crack detection based on structured prediction with the convolutional neural network. arXiv preprint arXiv:180202208. 2018.
- [20]. Dung CV. Autonomous concrete crack detection using deep fully convolutional neural network. *Automation in Construction*. 2019;99:52-8.
- [21]. Dorafshan S, Thomas RJ, Maguire M. Comparison of deep convolutional neural networks and edge detectors for image-based crack detection in concrete. *Construction and Building Materials*. 2018;186:1031-45.
- [22]. Cha YJ, Choi W, Büyükoztürk O. Deep learning-based crack damage detection using convolutional neural networks. *Computer - Aided Civil and Infrastructure Engineering*. 2017;32(5):361-78.
- [23]. Chen F-C, Jahanshahi MR. NB-CNN: deep learning-based crack detection using convolutional neural network and Naïve Bayes data fusion. *IEEE Transactions on Industrial Electronics*. 2018;65(5):4392-400.
- [24]. Yokoyama S, Matsumoto T. Development of an automatic detector of cracks in concrete using machine learning. *Procedia engineering*. 2017;171:1250-5.
- [25]. Tong Z, Gao J, Zhang H. Recognition, location, measurement, and 3D reconstruction of concealed cracks using convolutional neural networks. *Construction and Building Materials*. 2017;146:775-87.
- [26]. Cang R, Li H, Yao H, Jiao Y, Ren Y. Improving direct physical properties prediction of heterogeneous materials from imaging data via convolutional neural network and a morphology-aware generative model. *Computational Materials Science*. 2018;150:212-21.
- [27]. Wang S CH. A novel deep learning method for the classification of power quality disturbances using deep convolutional neural network[J]. *Applied energy*. 2019;235: 1126-1140.
- [28]. Li Y, Wang H, Mo K, Zeng T. Reconstruction of Simulation-Based Physical Field by Reconstruction Neural Network Method. 2018;arXiv preprint arXiv: 1811.02102.
- [29]. Li Y, Wang H, Deng X. Image-based reconstruction for a 3D-PFHS heat transfer problem by ReConNN. *International Journal of Heat and Mass Transfer*. 2019;134:656-67.
- [30]. Newmark NM. A method of computation for structural dynamics. *American Society of Civil Engineers*. 1959.
- [31]. Bengio Y MM, Larochelle H. Nonlocal Estimation of Manifold Structure. *Neural Computation*. 2006;18(10): 2509-2528.
- [32]. Kingma DP, Welling M. Auto-encoding variational bayes. arXiv preprint arXiv:1312.6114. 2013.
- [33]. Doersch C. Tutorial on variational autoencoders. arXiv preprint arXiv:1606.05908. 2016.

- [34].Osborne MJR, Ariel A Course in Game Theory. Cambridge, MA: MIT p 14 ISBN 9780262150415. 12 Jul 1994.
- [35]. Bishop CM. Pattern Recognition and Machine Learning. Springer. 2006.
- [36]. Harris DaH, Sarah. Digital design and computer architecture. San Francisco, Calif: Morgan Kaufmann. 2010;p. 129. ISBN 978-0-12-394424-5.
- [37]. Manning HSCD. Foundations of Statistical Natural Language Processing. Cambridge, Mass: MIT Press. 1999;p. 304. ISBN 978-0-262-13360-9.
- [38]. Arjovsky M, Chintala S, Bottou L. Wasserstein gan. arXiv preprint arXiv:170107875. 2017.
- [39]. Ledig C, Theis L, Huszár F, Caballero J, Cunningham A, Acosta A, et al., editors. Photo-realistic single image super-resolution using a generative adversarial network. Proceedings of the IEEE conference on computer vision and pattern recognition; 2017.
- [40]. Dong C, Loy CC, He K, Tang X. Image super-resolution using deep convolutional networks. IEEE transactions on pattern analysis and machine intelligence. 2016;38(2):295-307.
- [41]. Ghifary M, Kleijn WB, Zhang M, Balduzzi D, Li W, editors. Deep reconstruction-classification networks for unsupervised domain adaptation. European Conference on Computer Vision; 2016: Springer.
- [42]. Shi W, Caballero J, Huszár F, Totz J, Aitken AP, Bishop R, et al., editors. Real-time single image and video super-resolution using an efficient sub-pixel convolutional neural network. Proceedings of the IEEE conference on computer vision and pattern recognition; 2016.
- [43]. Goodfellow IJ, Pouget-Abadie J, Mirza M, Xu B, Warde-Farley D, Ozair S, et al., editors. Generative adversarial nets. International Conference on Neural Information Processing Systems; 2014.
- [44]. Mirza M, Osindero S. Conditional Generative Adversarial Nets. Computer Science. 2014:2672-80.
- [45]. Denton E L CS, Fergus R. . Deep Generative Image Models using a Laplacian Pyramid of Adversarial Networks. Advances in neural information processing systems. 2015;2015: 1486-1494.
- [46]. Goodfellow I, Mirza, M., Courville, A., and Bengio, Y. Multi-prediction deep boltzmann machines. Advances in Neural Information Processing Systems. 2013;pages 548–556.
- [47]. Welstead ST. Fractal and wavelet image compression techniques: SPIE Optical Engineering Press Bellingham, Washington; 1999.
- [48]. Wang Z, Bovik AC, Sheikh HR, Simoncelli EP. Image quality assessment: from error visibility to structural similarity. IEEE transactions on image processing. 2004;13(4):600-12.
- [49]. Peng Y, Wang X, Xiong X, Xu P. Crashing analysis and multi-objective optimisation of duplex energy-absorbing structure for subway vehicle. International journal of crashworthiness. 2016;21(4):338-52.
- [50]. Peng Y, Deng W, Xu P, Yao S. Study on the collision performance of a composite energy-absorbing structure for subway vehicles. Thin-Walled Structures. 2015;94:663-72.
- [51]. Hou S, Zhao S, Ren L, Han X, Li Q. Crashworthiness optimization of corrugated sandwich panels. Materials & Design. 2013;51:1071-84.
- [52]. Wang S, Peng Y, Wang T, Che Q, Xu P. Collision performance and multi-objective robust optimization of a combined multi-cell thin-walled structure for high speed train. Thin-Walled Structures. 2019;135:341-55.